R-06-48

Seismically induced slip on rock fractures

Results from dynamic discrete fracture modeling

Billy Fälth, Harald Hökmark
Clay Technology AB

November 2006

Svensk Kärnbränslehantering AB
Swedish Nuclear Fuel
and Waste Management Co
Box 5864
SE-102 40 Stockholm Sweden
Tel 08-459 84 00
+46 8 459 84 00
Fax 08-661 57 19
+46 8 661 57 19

ISSN 1402-3091
SKB Rapport R-06-48

Seismically induced slip on rock fractures

Results from dynamic discrete fracture modeling

Billy Fälth, Harald Hökmark
Clay Technology AB

November 2006

Keywords: Earthquake, Fracture slip, Rock, Numerical modeling, Glaciation, Fault, Dynamic effects, Stress drop, Repository, Canister damage.

Abstract

The possibility that glacially induced earthquakes in pre-existing faults may reactivate host rock fractures and induce fracture slip is considered in SKB's safety assessment. The specific concern is that fractures may intersect deposition holes and the question is raised if seismically induced fracture slip can damage the isolation capacity of the canister and thereby jeopardize the integrity of the barrier system. According to the present-day canister damage criterion applied by SKB, the slip in a fracture intersecting a deposition hole must not exceed 100 mm.

In the present study, the effects on rock fractures of an earthquake in a pre-existing fault are simulated. This is done by numerical modeling with *3DEC*. The modeling approach allows for the study of both dynamic and static effects. A steeply dipping fault is defined, along which a rupture is programmed to propagate according to a specified scheme. At different distances from the fault, numerous rock fractures with different orientations are set up. All fractures have 150 m radius and properties according to data from on-going site investigations. Two models simulating magnitude 6 events are analyzed. In one model, the rupture is buried, i.e. its upper edge is located below the ground surface. In the other model, the rupture breaches the ground surface.

The largest rock fracture slip found is 58 mm, which is well below the canister damage criterion. This fracture movement is found at 200 m distance from the fault. It can also be concluded that the distance between the fault and the fracture has great importance for the amount of induced fracture slip. At 600 m and 1,000 m distance, the shear displacements are in general significantly smaller than those found at 200 m distance. The maximum calculated fracture shear velocity is about 860 mm/s. The results also indicate that the dynamic effects are important for the triggering of fracture slip.

Sammanfattning

Möjligheten att glacialt inducerade skalv längs existerande förkastningar reaktiverar sprickor och ger upphov till spricksskjuvrörelser beaktas i SKB:s säkerhetsanalys. Specifikt intresserar man sig för att sprickor kan skära deponeringshål och frågan är om seismiskt inducerade skjuvrörelser kan förstöra kapselns isolerande förmåga och på så sätt äventyra barriärsystemets funktion. Enligt det kapselskadekriterium som för närvarande tillämpas av SKB får skjuvrörelsen i en spricka som skär ett deponeringshål inte överstiga 100 mm.

I denna studie simuleras effekterna på bergsprickor av ett jordskalv i en existerande förkastning. Detta görs genom numerisk modellering med *3DEC*. Det använda tillvägagångssättet medger att både dynamiska och statiska effekter kan studeras. En brantstående förkastning definieras, längs vilken ett brott programmeras att propagera enligt ett specificerat mönster. Ett stort antal sprickor med olika orientering och på olika avstånd från förkastningen definieras. Alla sprickor har 150 m radie och egenskaper enligt data från pågående platsundersökningar. Två modeller vilka simulerar magnitud 6-skalv analyseras. I en modell är förkastningssprickan dold, dvs. dess övre kant är belägen under markytan. I den andra modellen bryter förkastningen genom markytan.

Den största spricksskjuvrörelse som återfinns i modellerna är 58 mm, vilket är väl under kapselskadekriteriet. Denna sprickrörelse återfinns på 200 m avstånd från förkastningen. En slutsats som också kan dras är att avståndet mellan förkastning och spricka har stor betydelse för spricksskjuvrörelsens storlek. På 600 m och 1 000 m avstånd är skjuvrörelserna i allmänhet avsevärt mindre än de på 200 m avstånd. Den maximalt beräknade spricksskjuvhastigheten är ungefär 860 mm/s. Resultaten visar också på att de dynamiska effekterna är viktiga för att sprickrörelser skall kunna induceras.

Contents

1 Introduction and background

1.1 General

The concept for storing spent nuclear fuel applied by SKB is the KBS-3 system in which the spent fuel will be encapsulated in canisters consisting of a cast iron insert surrounded by a copper shell. The canisters will be deposited in vertical deposition holes in crystalline rock at approximately 500 m depth. They will be surrounded by a barrier of bentonite clay for isolation and mechanical protection. The fuel will be hazardous for very long times and the time perspectives applied in the safety assessment work are hundreds of thousands of years. This means that, within this time span, the repository is likely to be subjected to effects of future glaciations.

During a glaciation, the movements in the crust may result in accumulation of strain energy under the ice cover. When the ice disappears, excess strain energy may be released by seismic shear movements along large deformation zones. There is evidence that intensive seismic activity, glacially induced faulting, took place in Lapland in direct conjunction with the melting of the most recent ice cap (the Lansjärv Fault, the Pärvie Fault, etc) /Arvidsson 1996/. The seismic activity in the area might at some period of time have been comparable to the one in highly tectonically active areas such as plate boundaries /Muir Wood 1993/. The magnitude of the Lansjärv earthquake, for instance, is estimated to have been 7.8.

There is a possibility that glacially induced earthquakes along existing faults may induce secondary shear displacements along rock fractures at some distance from the fault. From the safety assessment point of view the concern is that such fractures may intersect a deposition hole and the question is raised if such seismically induced fracture shear movements can damage the isolation capacity of the canister and thereby jeopardize the integrity of the barrier system. According to the present-day canister damage criterion applied by SKB, the fracture shear movement must not exceed 100 mm /Hedin 2005/. The same criterion was applied in the previous SKB safety assessment /SKB 1999/.

1.2 Scope

The problem discussed above is considered in the present study. To make the presentation of the problem clear, it is summarized in Section 1.3. Together with the problem statement, some related questions are also listed. In the work, a number of specific parameters and concepts were used. Since they are essential for the understanding of the problem- and model descriptions, these are defined and discussed separately in Section 1.4.

Analyses of seismically induced rock fracture shear movements have also been performed in previous studies. The assumptions made in these studies and their implications for the results interpretation are discussed in Chapter 2.

In the present study, the assumptions made in the previous studies regarding the rock fracture properties are revised and more realistic parameter values are used. The models were analyzed by use of the 3-dimensional code *3DEC*. These models are described in Chapter 3 and the results from the analyses are presented in Chapter 4. In Chapter 5, the relevance and validity of the modeling approach is discussed. Results are compared with results from a similar model analyzed in a previous study and the limitations and the conservatism in the modeling approach are discussed. In Chapter 6, the results of this study are summarized and discussed, conclusions are made and further works are proposed.

1.3 Problem statement

The questions that are to be considered are:

- What is the static and dynamic impact of an earthquake upon nearby fractures in terms of induced slip?
- How does the induced slip correlate to the distance from the source?
- What is the importance of the fault geometry?

We address these questions by analysis of numerical models which were set up according to the following:

- A seismic dip slip event takes place in a pre-existing, steeply dipping fault. The fault is of reverse type, as was proposed for glacially induced faults observed in northern Fennoscandia /see e.g. Muir Wood 1993/.
- The earthquake is of magnitude 6 or larger.
- The fault may either:
  a. have a blind upper termination, i.e. its upper edge is located below the ground surface or
  b. breach the ground surface.
- At about 500 m depth, fractures are located at different distances from the fault.

1.4 Parameters and concepts

A number of parameters and concepts used in the model descriptions and in the results discussions are listed and explained below.

1.4.1 Primary fault

The primary fault is here used as notation for the geological formation along which the rupture process is taking place during the earthquake. In the models used here, this fault is represented by one discrete planar feature.

1.4.2 Target fracture

A rock fracture located in the vicinity of the primary fault and which potentially will be reactivated by the seismic event is here denoted target fracture. The amount of slip on such fractures is the main concern in this study.

1.4.3 Hypocenter and epicenter

The hypocenter is the location of the earthquake, i.e. the point at the primary fault where the rupture process is initiated. In the literature the hypocenter is also known as the focus of the earthquake. The epicenter is the point at the ground surface which is located above the hypocenter.

1.4.4 Stress drop

The shear stress reduction in the fault due to the primary fault slip during the earthquake is called stress drop.

1.4.5 Rise time

Here, rise time is defined as the time it takes for the stress drop to occur at any point on the primary fault. Some authors define rise time as the duration of the slip for a particular point, see e.g. /Scholz 1990, Stein and Wysession 2003/.

1.4.6 Wave propagation speed

The velocity C_p of compressional stress waves and the velocity C_s of shear stress waves in an elastic and homogenous medium are given by

$$C_p = \sqrt{\frac{K + 4/3G}{\rho}} \quad \text{m/s}$$
$$C_s = \sqrt{\frac{G}{\rho}} \quad \text{m/s} \tag{1-1}$$

where K is the bulk modulus, G is the shear modulus and ρ is the density of the medium. The values of K and G used for this study are listed in Table 1-1.

Table 1-1. Values of the bulk- and shear moduli.

Component	Unit	Value*
K	GPa	50
G	GPa	30

*) $K = \frac{E}{3-6\upsilon}$; $G = \frac{E}{2(1+\upsilon)}$ (E = 75 GPa and v = 0.25, cf Table 3-3).

1.4.7 Moment magnitude and seismic moment

Magnitude is a dimensionless parameter used to quantify the size of an earthquake. The earliest magnitude scale was the local magnitude, M_L, introduced by Charles Richter in 1935 for earthquakes in southern California. It is often referred to as the "Richter scale" and is based on the resulting amplitude of waves that are recorded on a seismogram and on functions that are calibrated to account for regional conditions. Other magnitude scales have also been developed. For global studies, the two primary scales used are the body wave magnitude, m_b and the surface wave magnitude, M_s. These scales are also based on measurements of ground motion amplitudes. One limitation of these scales is that they saturate, i.e. for earthquakes with seismic moments above a certain level, they do not increase even if the seismic moment increases /Stein and Wysession 2003/. Another scale which has become the common measure of large earthquakes is the moment magnitude, M_w. This scale is based on the seismic moment, M_0, and it does not saturate for large earthquakes. The moment magnitude has been applied in this work and is defined as:

$$M_w = \frac{2}{3} log_{10} M_0 - 6.07 \tag{1-2}$$

The seismic moment M_0 is calculated as

$$M_0 = G\bar{U}A \tag{1-3}$$

where G is the shear modulus and $\bar{U}$ is the average slip along the rupture area A.

1.4.8 Stress sign convention

According to the stress sign convention applied in this study, tensile stresses are positive and compressive stresses are negative.

2 Previous work

2.1 General

The problem considered in the present report has been addressed in previous studies. Here, brief descriptions of the different approaches that have been used are given.

2.2 Static approach

The earthquake scenario in the risk analysis in the SR 97 safety report /SKB 1999/ is based on estimates of target fracture shear movements due to effects of earthquakes performed by /La Pointe et al. 1997/. The code used in that work is a Displacement Discontinuity code called Poly3D. The modeling was based on the assumption that the static stress redistribution resulting from an earthquake gives the dominating contribution to the target fracture movements, i.e. that oscillatory components can be ignored. A magnitude 6 earthquake occurring at 2 km distance from the edge of the repository was simulated with a static analysis Figure 2-1 (left). Numerous frictionless, circular target fractures with different sizes and orientations were distributed in the medium according to a statistical Discrete Fracture Network (DFN) model.

The results from the study were presented as the maximum shear displacement of the target fractures versus target fracture size (Figure 2-1, right). However, the interpretation of the results was not straightforward since the target fractures had varying sizes and orientations. /Munier and Hökmark 2004/ estimated the maximum displacement on 100 m radius fractures by using the worst case size-displacement ratio found among the results. The calculation suggested that the maximum shear displacement of 100 m radius, friction-free fractures at 2 km distance from the fault would be 12–13 mm.

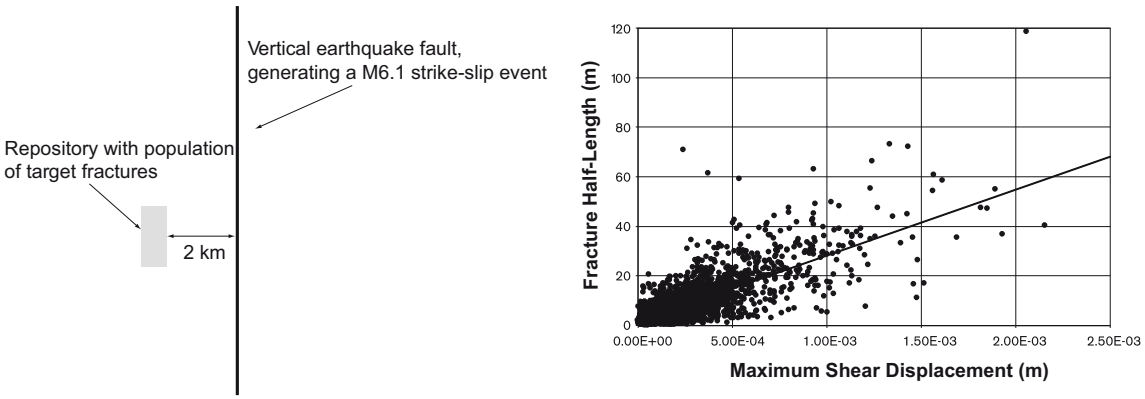

Figure 2-1. *Left: Schematic plan view of repository volume and earthquake fault. Right: Relation between induced displacement and fracture size. From /Munier and Hökmark 2004, Figures 3-3 and 3-4/.*

2.3 Dynamic approaches

Dynamic analyses of seismic events have also been performed in order to estimate possible induced target fracture slip. /Munier and Hökmark 2004/ report results from three modeling approaches where magnitude 6 events have been simulated:

1. Models analyzed in *FLAC3D* where dynamic boundary conditions were applied at the bottom of the model such that all the base points moved together. The boundary conditions were obtained from an analysis in the code WAVE. Both friction- and non-friction target fracture cases were studied. Only dynamic effects on the target fractures were considered in these models. A limitation is that the plane wave assumption made in this approach is valid only for large source–target distances.
2. WAVE models including both primary fault and target fractures. The earthquake was simulated by prescription of shear displacements along the primary fault. Both dynamic and static effects were considered and both friction-free target fractures and target fractures with friction were studied. Due to limitations in the code, the target fractures and the primary fault had to be aligned to the same Cartesian coordinate system. Thus, the orientation of the target fractures could not be chosen arbitrarily and the fault had to be either horizontal or vertical.
3. *FLAC3D* analyses, where both primary fault and target fracture were included. Both dynamic and static effects considered. Both friction- and non-friction target fracture cases were studied. Only one target fracture at a relatively large distance from the fault was studied.

In some of the modeling approaches described above, the effect of target fracture friction was considered. However, the parameter values that were used correspond to a shear strength that is low compared to what is measured in fracture samples from SKB's candidate sites. In the models with fracture friction, a Mohr-Coulomb model with a maximum friction angle of 15° was used. This is about half of the values measured in the site investigations /SKB 2005ab, 2006/ and thus it is likely that the target fracture movements were overestimated in the simulations.

3 3DEC modeling approach

3.1 General

The models were analyzed by use of *3DEC*, which is a three-dimensional code based on the distinct element method /Itasca 2003/. The modeling approach applied was to analyze models where both the primary fault and the target fractures were included. In situ stress conditions were defined that resulted in an approximate average initial shear stress of 15 MPa along the primary fault. The earthquake was then generated by a programmed reduction of the fault shear strength, resulting in fault slip and accompanying strain energy release. After completed rupture the fault strength had reached zero, giving an average net stress drop of 15 MPa.

The modeling approach made it possible to study the target fracture displacements due to both static stress redistributions and dynamic oscillation effects. Two models were analyzed (Figure 3-1):

1. *Case A:* Model where the upper edge of the fault is located 1,000 m below the ground surface. The primary fault geometry was similar to the *FLAC 3D* model used in the "step 3"-analysis reported by /Munier and Hökmark 2004/.
2. *Case B:* Similar to *Case A*, but with an extended fault breaching the ground surface.

3.2 Geometry

3.2.1 Geometric outlines

A model overview is shown in Figure 3-2. Model dimensions are given in Table 3-1. The upper boundary of the models represents the ground surface. The target fractures are located at 500 m depth. The majority of the cuts seen in the figure correspond to mechanically invisible construction planes. These were used to define the geometry and to facilitate the discretization of the continuum. Only some of the cuts correspond to planes of real fractures (cf Figure 3-3).

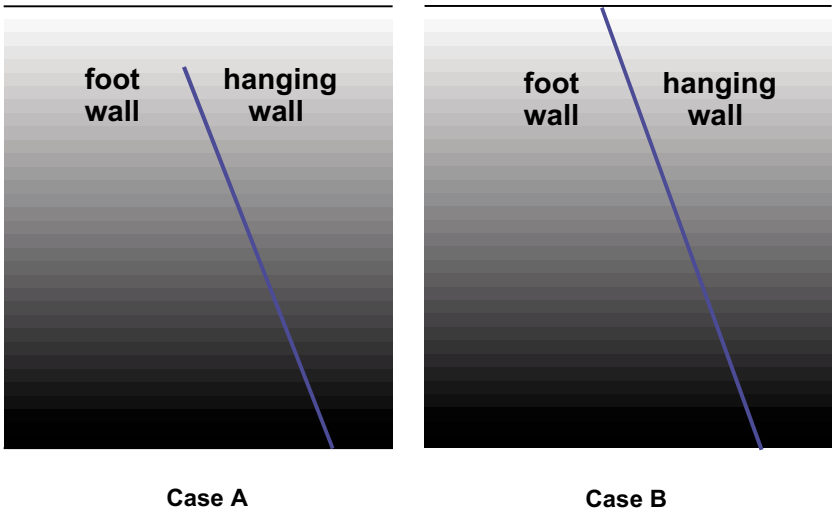

Figure 3-1. *Explanatory sketches illustrating the difference between the models. Left: Case A, with buried rupture. Right: Case B, with ground surface breaching rupture.*

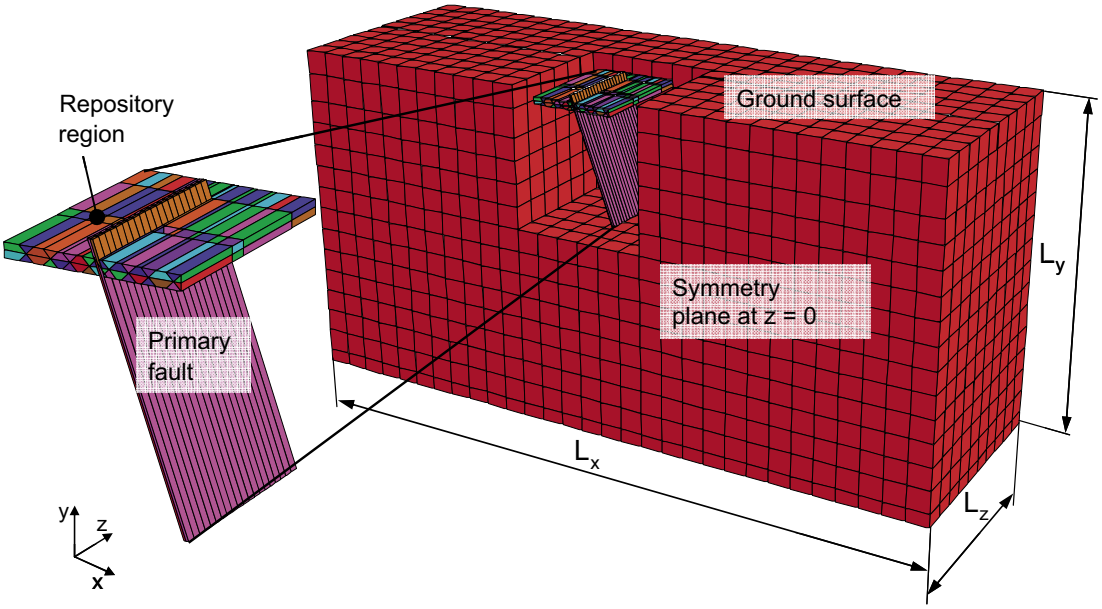

Figure 3-2. *Geometric outlines of the model. To show the primary fault plane and the repository region, some parts of the model are hidden. The picture is taken from Case B where the primary fault breaches the ground surface. Note that the majority of the cuts seen in the figure correspond to mechanically invisible construction planes. These were used to define the geometry and to facilitate the discretization of the continuum.*

Table 3-1. Model's outer dimensions.

	L_x	L_y	L_z	Unit
Case A	16,000	9,000	8,000	m
Case B	30,000	15,000	10,000	m

The dimensions of the models had to be large enough to ensure that the static part of the fault movement was not influenced by the boundaries. The dimensions of the primary fault were (Length x Width) 4 x 4.6 km^2 in *Case A* and 4 x 5.6 km^2 in *Case B*. The boundary at z = 0 was set to be a symmetry plane, i.e. no displacements normal to the plane allowed. Thus, the models simulated a fault length of 8 km.

3.2.2 Target fractures

The target fractures were defined by assigning target fracture properties to specific sub-contacts such that circular fractures were formed. This was done with *FISH,* which is a built-in programming language in *3DEC* /Itasca 2003/. The principle used for this procedure is illustrated in Figure 3-3. A fracture was defined as the circular area created by the intersection between two geometric entities:

1. A sphere with its center located in the center of the fracture and with its radius equal to that of the fracture.
2. A *3DEC* cut plane intersecting the center point of the sphere and with intended dip and dip direction angles.

This circular area was assigned with target fracture properties according to Table 3-3. The remaining area of the cut plane was assigned with fictitious fracture strength properties to prevent slip.

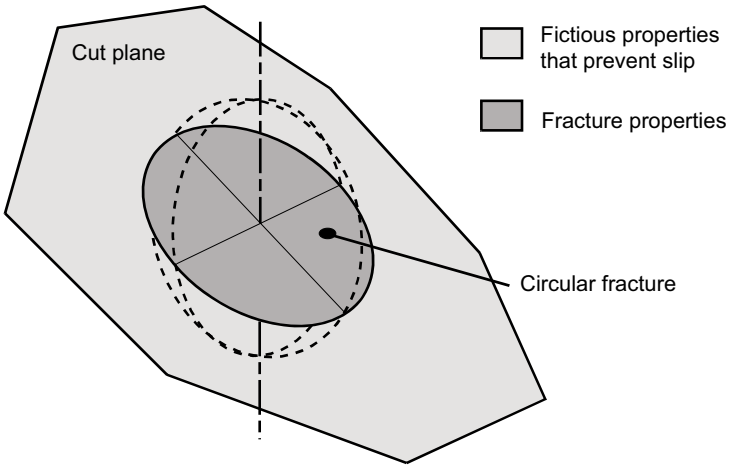

Figure 3-3. *The principle used for defining a circular fracture in an arbitrary 3DEC cut plane. The circular fracture was defined as the intersection between a sphere and the cut plane.*

A large number of target fractures at different distances from the fault and at different distances from the symmetry plane were included, all located at 500 m depth (Figure 3-4). Both horizontal target fractures and target fractures dipping 45° were defined. The left picture shows the horizontal cut plane at which the horizontal target fractures were located and the cut planes of the dipping target fractures. The picture also shows the primary fault, which has dip direction 90 degrees (dip directed along positive x-axis). Target fractures with dip direction 90 degrees as well as fractures with dip direction 270 degrees (dip directed along negative x-axis) were defined. All target fracture radii were 150 m. In order to limit the complexity of the models, all target fractures had the same strike as the primary fault and no vertical target fractures were defined. Slip in vertically oriented fractures will also be less hazardous to vertically deposited canisters. To the right, an overview of the target fracture locations is shown. Fractures are shown as circles, irrespective of dip. The dotted line indicates the location of the primary fault. The fractures were located at four x-distances on both sides of the fault and at twelve z-distances,

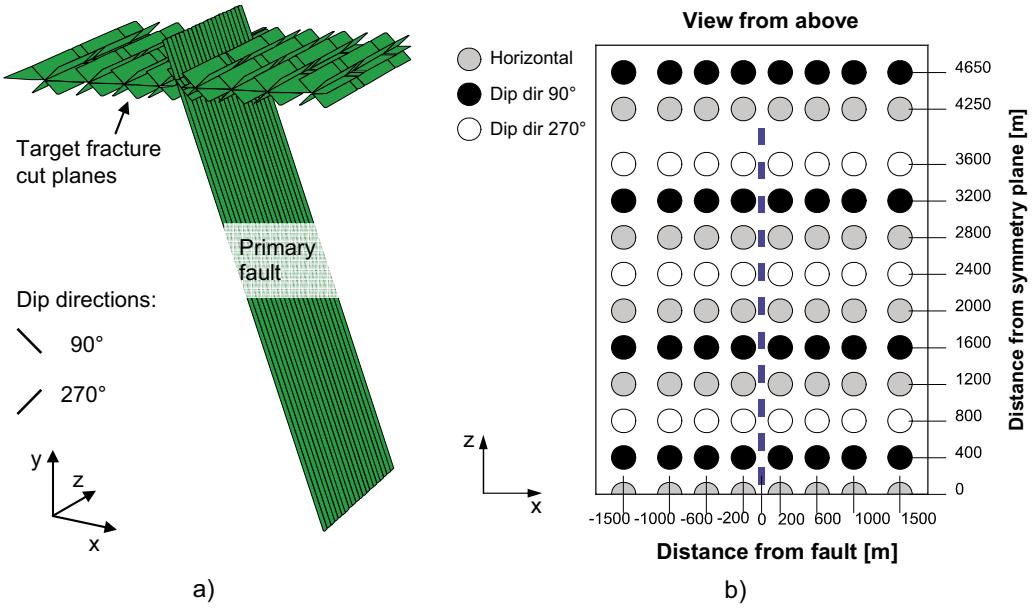

Figure 3-4. *Target fracture locations and orientations. Picture a) shows the horizontal and dipping cut planes in which the circular target fractures where defined as shown in Figure 3-3. The picture also shows the primary fault plane, which has dip direction 90°. Picture b) is an explanatory sketch of the target fracture locations and orientations. Fractures are shown as circles, irrespective of dip.*

i.e. at different distances from the symmetry plane. The fractures with z-coordinates 4,250 and 4,650 were located beyond the primary fault's vertical edge. All target fractures responded to loads according to an idealized elasto-plastic material model with a 34° friction angle and 0.5 MPa of cohesion.

In addition to the target fractures shown in Figure 3-4, a few particular target fractures were defined. In *Case A,* there was a horizontal frictionless target fracture located at 2,000 m horizontal distance from the upper edge of the fault (2,800 m from epicenter) (Figure 3-5, left). The shear displacements of this fracture was compared with corresponding results from the step 3 *FLAC 3D* analysis reported by /Munier and Hökmark 2004/ (cf Section 5.2). In *Case B*, four fractures intersecting the primary fault were set up at the z-coordinates 0, 400, 3,600 and 4,250 m, respectively. Their centers were located at 34 m horizontal distance from the fault and they had a dip angle of 50° and dip direction 90° (Figure 3-5, right).

3.2.3 Finite difference element mesh

To ensure proper wave transmission through the continuum, the finite difference zone edge lengths Δl must not be larger that one-eighth of the wave length associated with the highest frequency /Itasca 2003/, i.e.

$$\Delta l \leq \frac{1}{8}\frac{C}{f} \qquad (3\text{-}1)$$

Here, C is the wave propagation speed and f is the highest frequency in the spectrum. The mechanical properties assumed here give a shear wave propagation speed C_s of 3,333 m/s (cf Equation 1-1).

The outlines of the meshes in the two models are shown in Figure 3-6 and mesh data are presented in Table 3-2. In the repository volume where the target fractures were located and along the primary fault, the models were specifically densely meshed. The rock volume *Region 1*, which surrounds the primary fault and the repository volume, was discretized such that no edge lengths exceeded 400 m. According to Equation 3-1, this would ensure proper wave transmission of frequencies up to about 1 Hz in this volume. Due to memory allocation limitations in the computer system, this mesh density could not be set in *Region 2*. In these parts, a coarser meshed was used, cf Table 3-2. However, this only influences the stress wave transmission in distant parts where the dynamic response has little importance for the main results in the central parts of the models. The large volume of *Region 2* was incorporated mainly to prevent the boundaries from influencing the static parts of the results. Both models (A and B) included about 1000,000 finite difference zones.

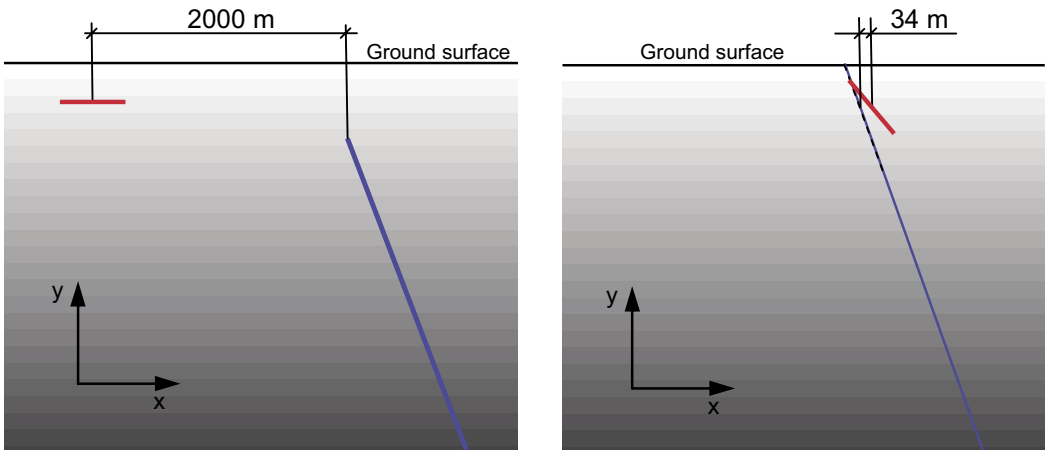

Figure 3-5. *Additional target fractures. Left: Location of the frictionless horizontal target fracture in Case A. This fracture was used in a benchmark test. Right: Location of target fractures intersecting the fault in Case B.*

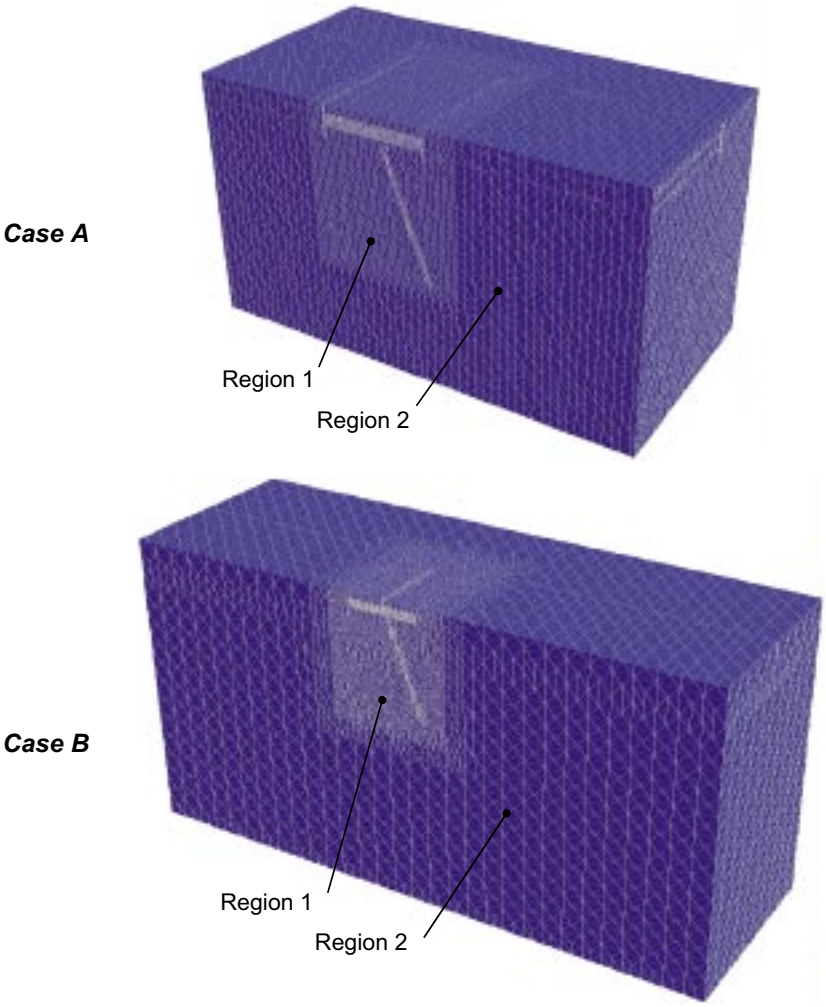

Figure 3-6. *The figure shows outlines of the meshes in the two models. Region 1 one was meshed using zone edge lengths that ensure proper wave transmission of frequencies up to 1 Hz. In region 2, the mesh was allowed to be coarser.*

Table 3-2. Zone sizes.

Maximum zone size [m]			
Target fracture volume	Along primary fault	Region 1	Region 2
117	125	392	1,890

3.3 Material properties

The material property parameter values are presented in Table 3-3. The rock was assumed to be linearly elastic and the fractures to respond to loads according to an idealized elasto-plastic material model with linear joint stiffness, zero tensile strength and shear failure according to a Coulomb criterion. The parameter values of the rock mass are the same as those used in the step 3 *FLAC 3D* analysis reported by /Munier and Hökmark 2004/. The values of Young's modulus and Poisson's ratio are generic, but are in good agreement with the values measured at SKB's candidate sites. The values of friction angle and cohesion for the target fractures are the same as those derived from the site models /SKB 2005ab, 2006/ by /Fälth and Hökmark 2006/.

Table 3-3. Material property parameter values.

Component	Parameter	Value	Unit
Rock mass	Density ρ	2,700	kg/m^3
	Young's modulus E	75	GPa
	Poisson's ratio ν	0.25	–
Primary fault	Friction angle	0	deg
	Cohesion	0 (final, after completed rupture)	MPa
	Tensile strength	0	MPa
	Normal stiffness	10	GPa/m
	Shear stiffness	10	GPa/m
Target fractures	Friction angle	34	deg
	Cohesion	0.5	MPa
	Tensile strength	0	MPa
	Normal stiffness	10	GPa/m
	Shear stiffness	10	GPa/m

3.4 Calculation sequence

The simulations comprised two main calculation steps.

3.4.1 Static step

In situ stresses were applied (cf Section 3.5) and the model was allowed to achieve complete static equilibrium under gravity. High cohesive strength in the primary fault prevented it from slipping during this phase.

3.4.2 Dynamic step

The scheme used for rupture initiation and propagation, i.e. rise time, propagation speed and location of hypocenter, was proposed and used in a WAVE analysis reported by /Munier and Hökmark 2004/. The rise time was considered to be realistic and computationally advantageous. Tests performed in that study showed that, within reasonable limits, the rise time has little effect on the measured velocity field. The scheme was also used in the step 3 *FLAC 3D* analyses, also reported in /Munier and Hökmark 2004/. The following main parameter values were used:

- *Rise time:* 0.5 seconds.
- *Rupture propagation speed:* $0.7 \cdot C_s$
- *Hypocenter location:* At 3.16 km depth below the ground surface at the symmetry plane (z = 0). (This shallow focal depth is a consequence of the shallow earthquake geometry.)

3.5 Modeling the rupture

The rupture was initiated and programmed to propagate along the primary fault according to a specified scheme as detailed further below. The routine that was used to control rupture initiation and propagation was developed in *FISH*, which is a built-in programming language in *3DEC* /Itasca 2003/. The rupture was initiated at 3.16 km depth and the rupture front was programmed to move outwardly in a radial direction at a speed of 70% of the rock mass shear wave velocity (Figure 3-7). At every time step, each sub-contact in the fault was checked for shear stress and assigned a cohesive strength equal to the shear stress acting at that particular location. As the rupture front passed, the cohesive strength was ramped down to zero over a period of 0.5 seconds. The zero residual shear strength resulted in a stress drop that equals the initial shear stress, i.e. about 15 MPa on average. The duration of the rupture process was about 2 seconds, while the dynamic effects were simulated for a total of 10 seconds.

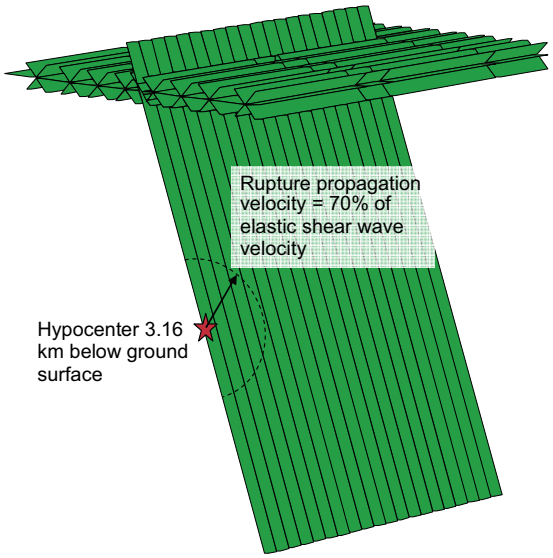

Figure 3-7. *Location of the hypocenter and propagation of the rupture.*

3.6 Initial conditions

The initial conditions are listed in Table 3-4. Initial stresses, varying with the depth below the ground surface, were defined. The stress state was identical to that used in the previous step 3 *FLAC 3D* analysis /Munier and Hökmark 2004/. The intention was to generate an average initial shear stress in the fault of 15 MPa. This is a value which is consistent with values of stress drop suggested for intraplate earthquakes /Scholz 1990/. In Figure 3-8 it is shown how the shear stress in the fault varies with depth before the rupture initiates. The same initial stress state was used in both cases. This resulted in a somewhat lower average shear stress in *Case B,* where the fault breaches the ground surface. In *Case A,* the average shear stress was 15 MPa and in *Case B* it was 13 MPa.

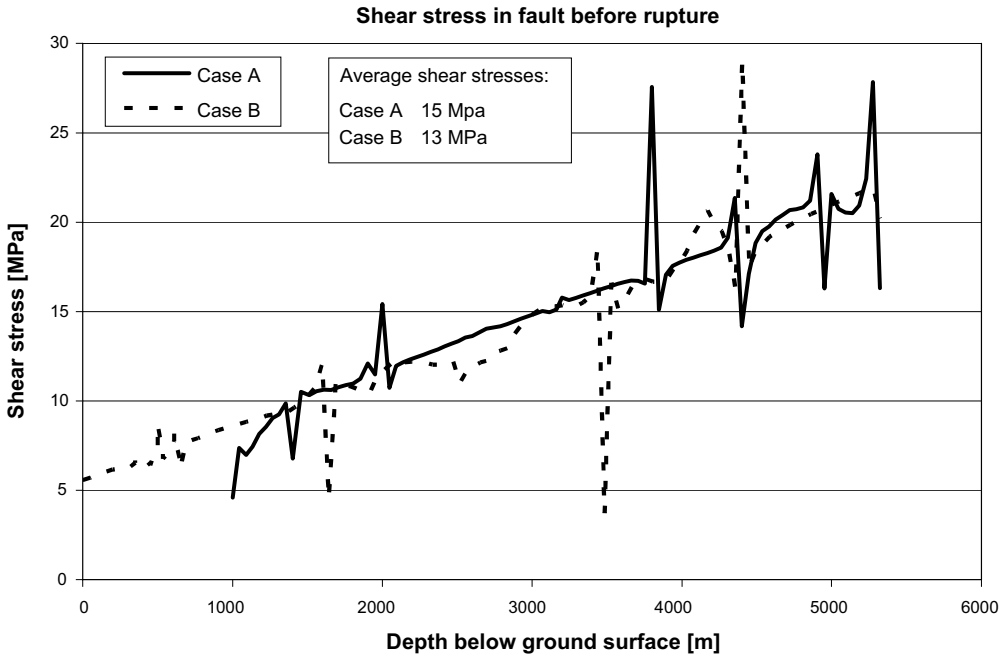

Figure 3-8. *Fault shear stress versus depth before rupture initiation. The stress peaks are anomalies which appear at block edges. They do not have any importance for the results*

Table 3-4. Initial conditions.

Component	Unit	Value	Comment
σ_x	MPa	17.25+0.0361*y	Horizontal stress perpendicular to the primary fault strike
σ_y	MPa	ρ*g*y = 0.026487*y	Vertical stress
σ_z	MPa	4.31+0.0156*y	Horizontal stress parallel to the primary fault strike
Fracture pore pressure	MPa	5	Constant through analysis
Gravity g	m/s^2	9.81	

3.7 Boundary conditions

In Figure 3-9, the boundary conditions are shown. The vertical boundary at z = 0 was a symmetry plane. Thus, this boundary was locked for displacements in the normal direction (roller boundary) for the duration of the analysis. At all the other vertical boundaries and the bottom boundary, roller boundary conditions were set during the static phase. During the dynamic phase, these boundaries were set to act as non-reflecting (viscous) boundaries. This kind of boundary condition prevents the boundaries from reflecting waves back into the model. The top boundary was a free boundary, allowing for surface reflection.

The viscous boundary conditions eliminate irrelevant reflections, but there is a risk that they give undesired static contributions to the results. The reaction forces acting at the boundaries at the end of the static phase are maintained by the viscous boundaries during the dynamic phase. This is a consequence of how viscous boundary conditions are formulated in *3DEC*. As the primary fault slips and the stresses in the model are relaxed, the boundaries are automatically moved into the model in order to maintain the stress at the boundary. If the model is too small, this may result in overestimated shear movements in the fault. This is the reason why the *Case B* model, where the fault breaches the ground surface, required larger dimensions than *Case A*. The breaching fault generates more displacements and consequently more extensive stress relaxations in the model.

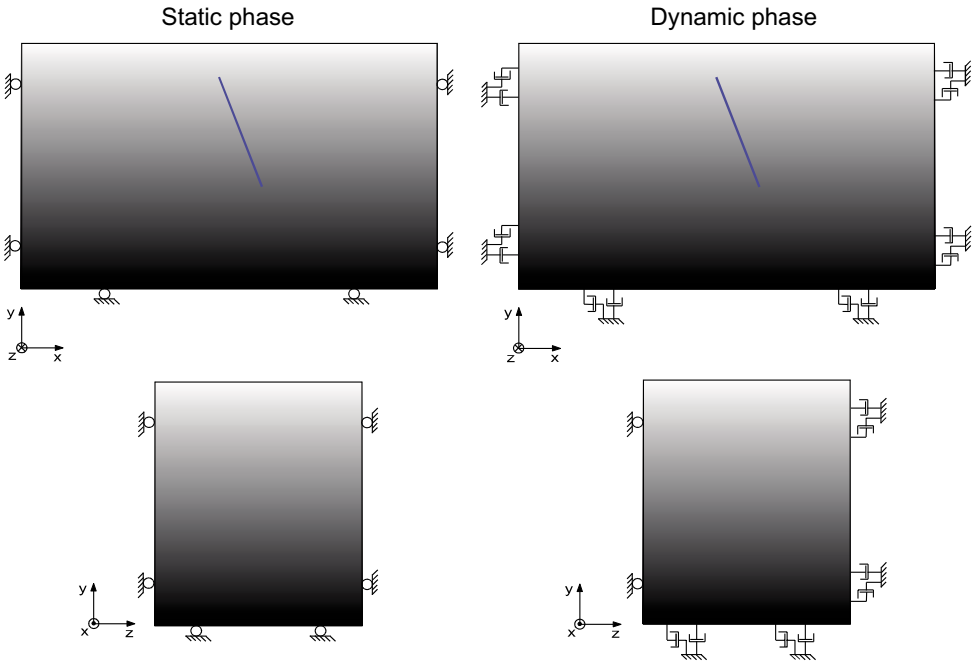

Figure 3-9. *Boundary conditions. The roller boundary conditions used during the static phase were switched into viscous (non-reflecting) boundaries during the dynamic phase. The roller boundary condition was kept at z = 0 (symmetry plane).*

4 Results

4.1 Primary fault slip and earthquake magnitude

The resulting values of primary fault slip and earthquake magnitude are presented in Table 4-1. The magnitudes of the earthquake were determined after completed rupture by summing the seismic moments for all sub-contacts on the primary fault surface and then converting the moment sum into moment magnitude (cf Equation 1-2). The displacements are considerably larger in *Case B* due to that the rupture breaches the ground surface in this case. In *Case A*, the primary fault slip is limited by the upper edge of the fault 1,000 m below ground surface.

Figure 4-1 shows results from *Case A*. The time development of the shear stress at four points in the primary fault is shown. The points were located at the hypocenter depth (3.16 km) and at different z-coordinates. The curves illustrate how the rupture front propagates outwardly from the hypocenter; the shear stress reduction starts at different instances of time at the different locations. The curves also show how the shear strength at each location is ramped down during a time of approximately 0.5 seconds. The rupture process is identical in *Case B*.

Table 4-1. Resulting primary fault slip and moment magnitudes.

	Unit	Case A	Case B
Maximum fault slip	m	1.9	3.0
Average fault slip	m	1.2	1.9
Seismic moment	Nm	$1.3 \cdot 10^{18}$	$2.6 \cdot 10^{18}$
Moment magnitude	–	6.0	6.2

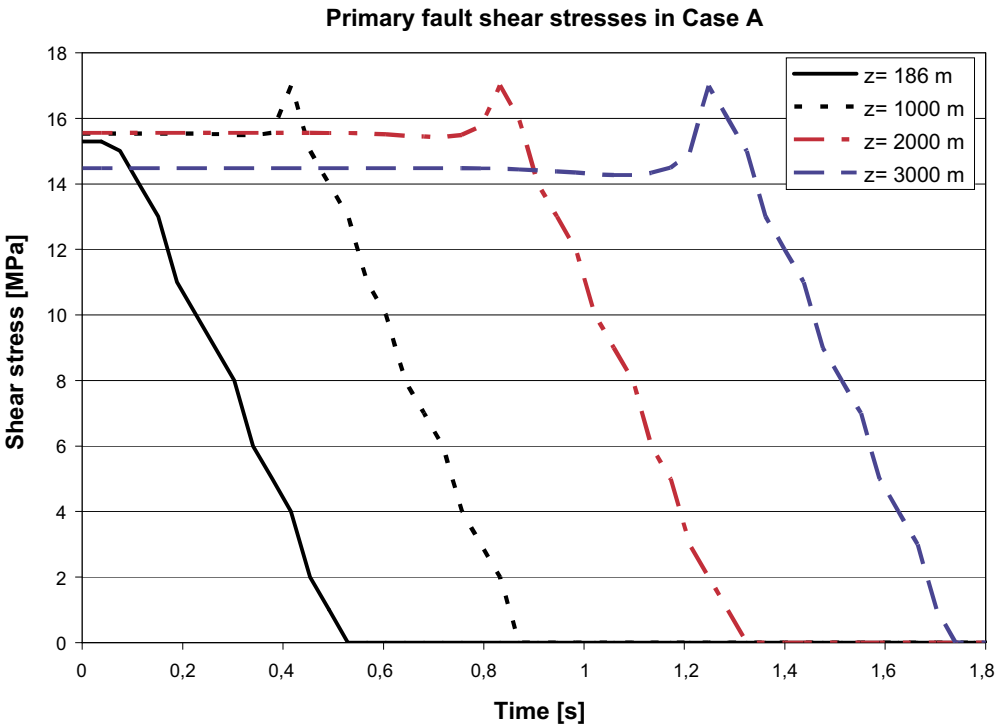

Figure 4-1. *The figure shows the time development of shear stress at four points in the primary fault. The points were located at the hypocenter depth (3.16 km) and at different z-coordinates.*

In Figure 4-2, results from the same four points that were considered in Figure 4-1 are shown. To the left, *Case A* results are shown whereas the diagram to the right shows *Case B* results. The diagrams show the time development of the primary slip at the four points. The slip starts at different times at the different points as the rupture front propagates. This is in agreement with the stress results shown in Figure 4-1. The diagrams also show the larger amounts of slip found in *Case B.*

The difference in the amount of primary slip between the two cases is also illustrated in Figure 4-3 and Figure 4-4. In Figure 4-3, the resulting slip versus depth below the ground surface is plotted. The target fracture that intersects the primary fault close to the ground surface in *Case B* gives a small local fault slip increase. In Figure 4-4, vector plots of the primary fault slip are shown. The plots regard three instances of time (0.5 s, 1 s and 10 s) after rupture initiation. The vectors are colored according to the vector magnitude. Figure 4-3 and Figure 4-4 both show the difference in the distribution of the slip, which is a result of the different primary fault geometries. In *Case B,* with no upper edge limiting the movement, the largest primary slip is found close to the ground surface whereas the maximum in *Case A* is found close to the hypocenter.

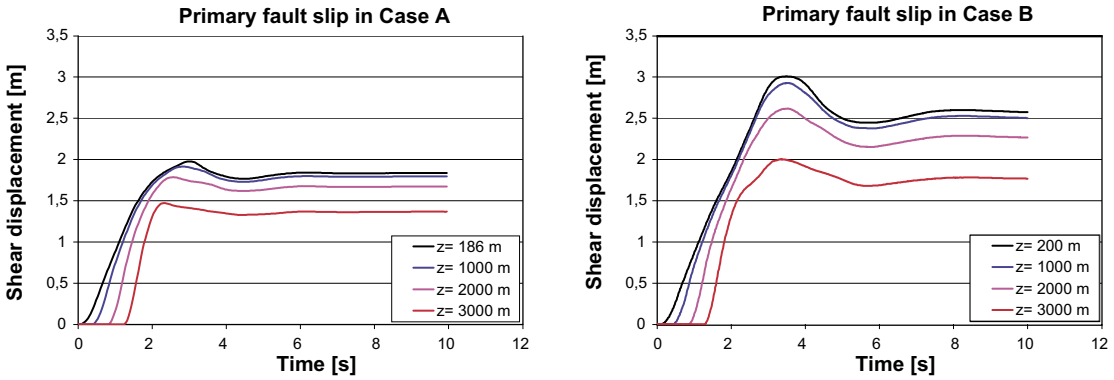

Figure 4-2. *Time development of the slip at four points in the primary fault. The points were located at the hypocenter depth (3.16 km) and at different z-coordinates. The diagrams show results from Case A (left) and Case B (right).*

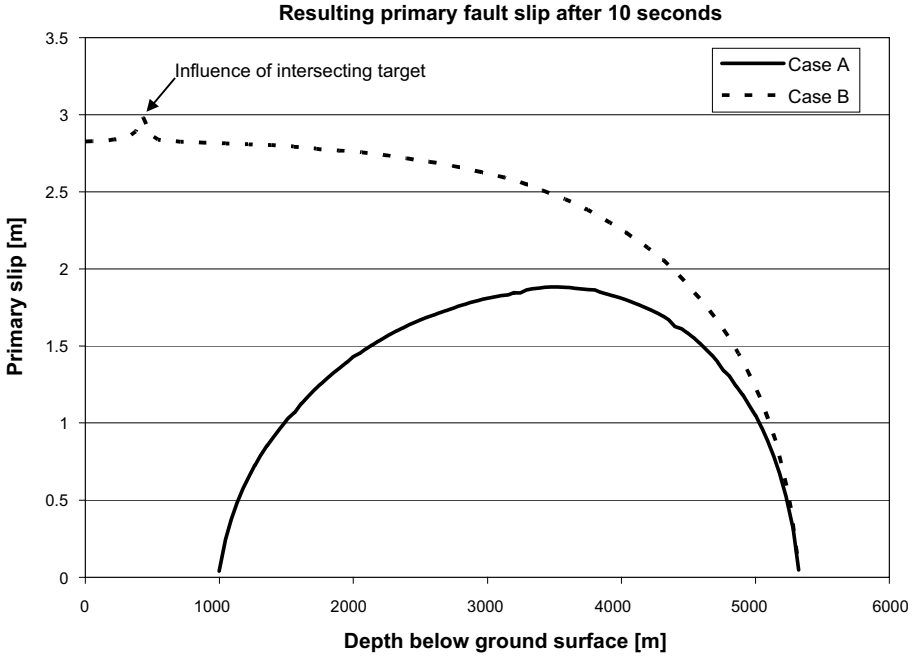

Figure 4-3. *Resulting primary fault slip after 10 seconds along the symmetry plane (z = 0).*

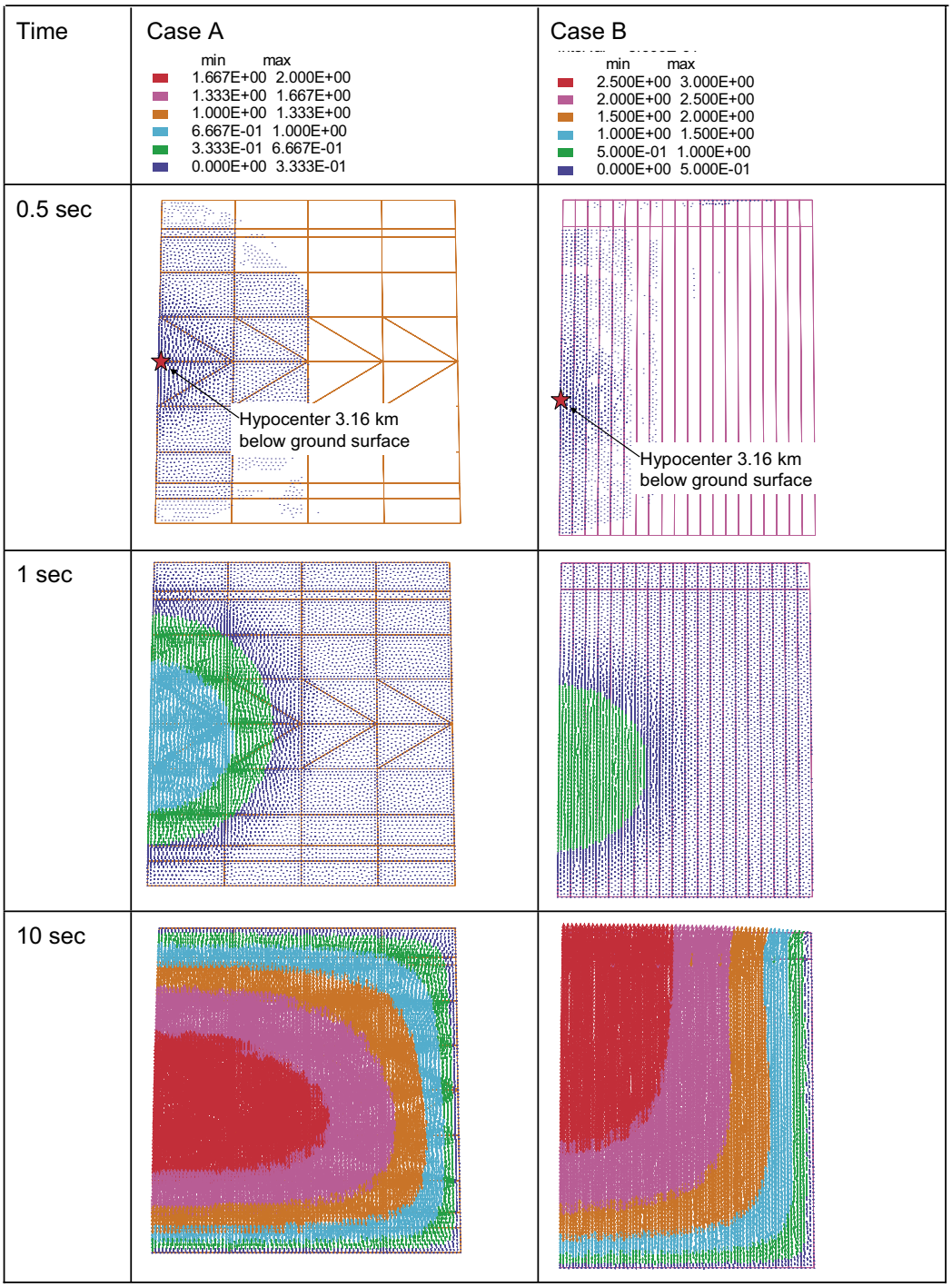

Figure 4-4. *Slip along primary fault at three instances of time. The vectors are colored according to their magnitude. Note the difference in fault height-width ratio between the two models due to larger vertical extension of the fault surface in Case B.*

4.2 Rock deformations and stresses

Above, the differences between the models regarding distribution and amount of primary fault slip were discussed. These differences were due to the difference in the primary fault geometry. The geometry has importance also for the rock deformations and the resulting stress changes. In Figure 4-5, rock deformations in *Case A* at three instances of time are shown and in Figure 4-6, corresponding results for *Case B* are shown. The importance of the fault geometry on the rock deformations becomes particularly clear if the states at 10 seconds are compared.

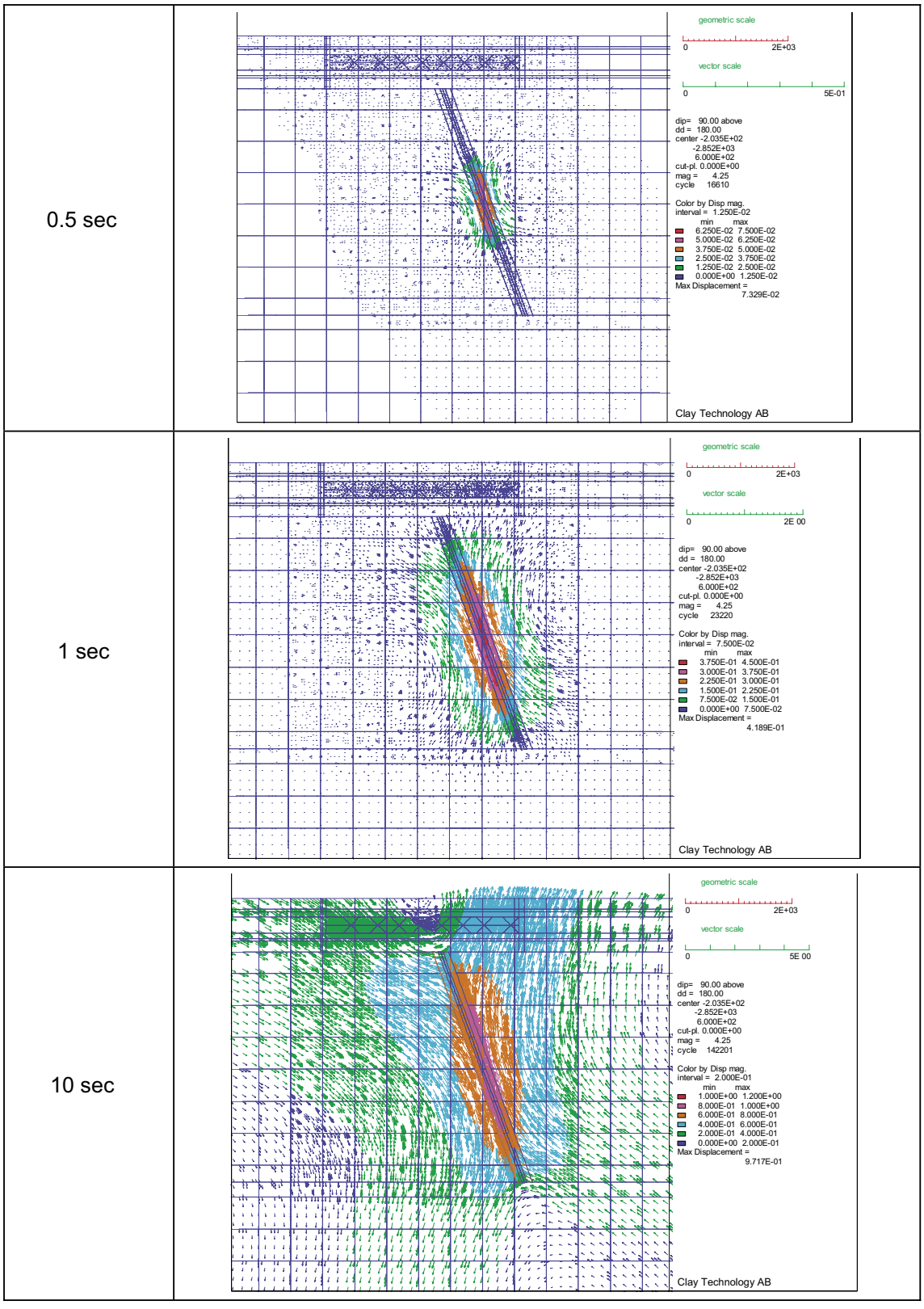

Figure 4-5. *Rock displacements in Case A at 0.5, 1 and 10 s. The vertical section is located at z = 600 m. The vectors are colored according to their magnitude.*

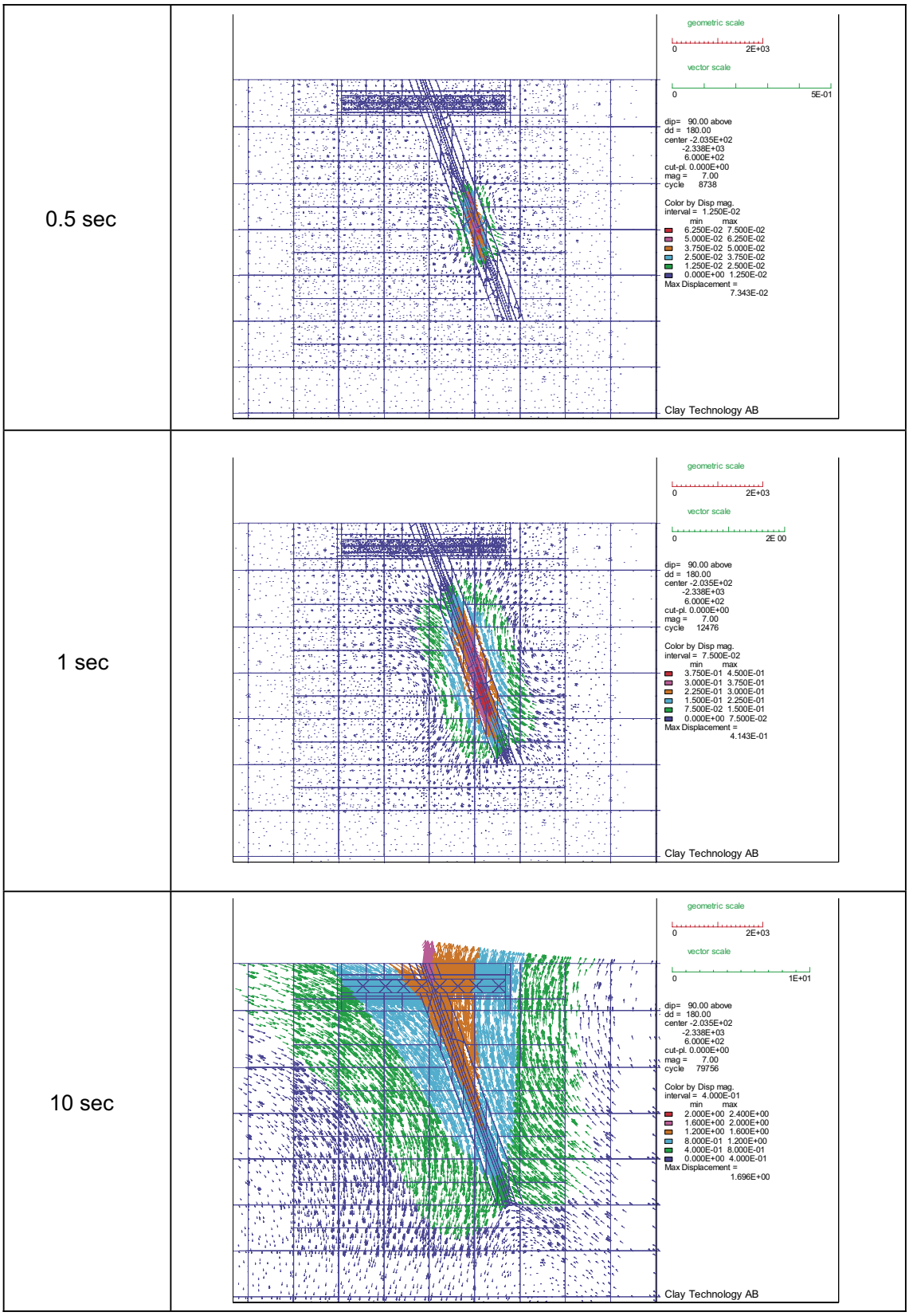

Figure 4-6. *Rock displacements in Case B at 0.5, 1 and 10 s. The vertical section is located at z = 600 m. The vectors are colored according to their magnitude.*

The upper edge of the fault in *Case A* limits the movement (Figure 4-5, bottom). It is also clear that larger rock volumes are affected in *Case B*. At the left edge of the pictures, the color scale (green) indicates displacements of 0.2–0.4 m in *Case A* and 0.4–0.8 m in *Case B*.

The resulting stress change at every point was calculated as

$$\Delta\boldsymbol{\sigma}_{i,j} = \boldsymbol{\sigma}_{i,j}\,(t = 10) - \boldsymbol{\sigma}_{i,j}\,(t = 0) \qquad (4\text{-}1)$$

where

$\boldsymbol{\sigma}_{i,j}\,(t = 10)$ is the stress state at time t = 10 s (end of analysis) and

$\boldsymbol{\sigma}_{i,j}\,(t = 0)$ is the stress state before rupture initiation.

Figure 4-7 shows stress additions in *Case A* after completed rupture. Since compressive stresses are negative in *3DEC,* positive stresses indicate compressive stress decrease (stress relaxation). In *Case A* the main slip generates stress concentrations around the edge and a complicated pattern of stress changes at 500 m depth. This is illustrated by the upper figure which shows principal stress tensor symbols colored according to the largest compressive stress increase.

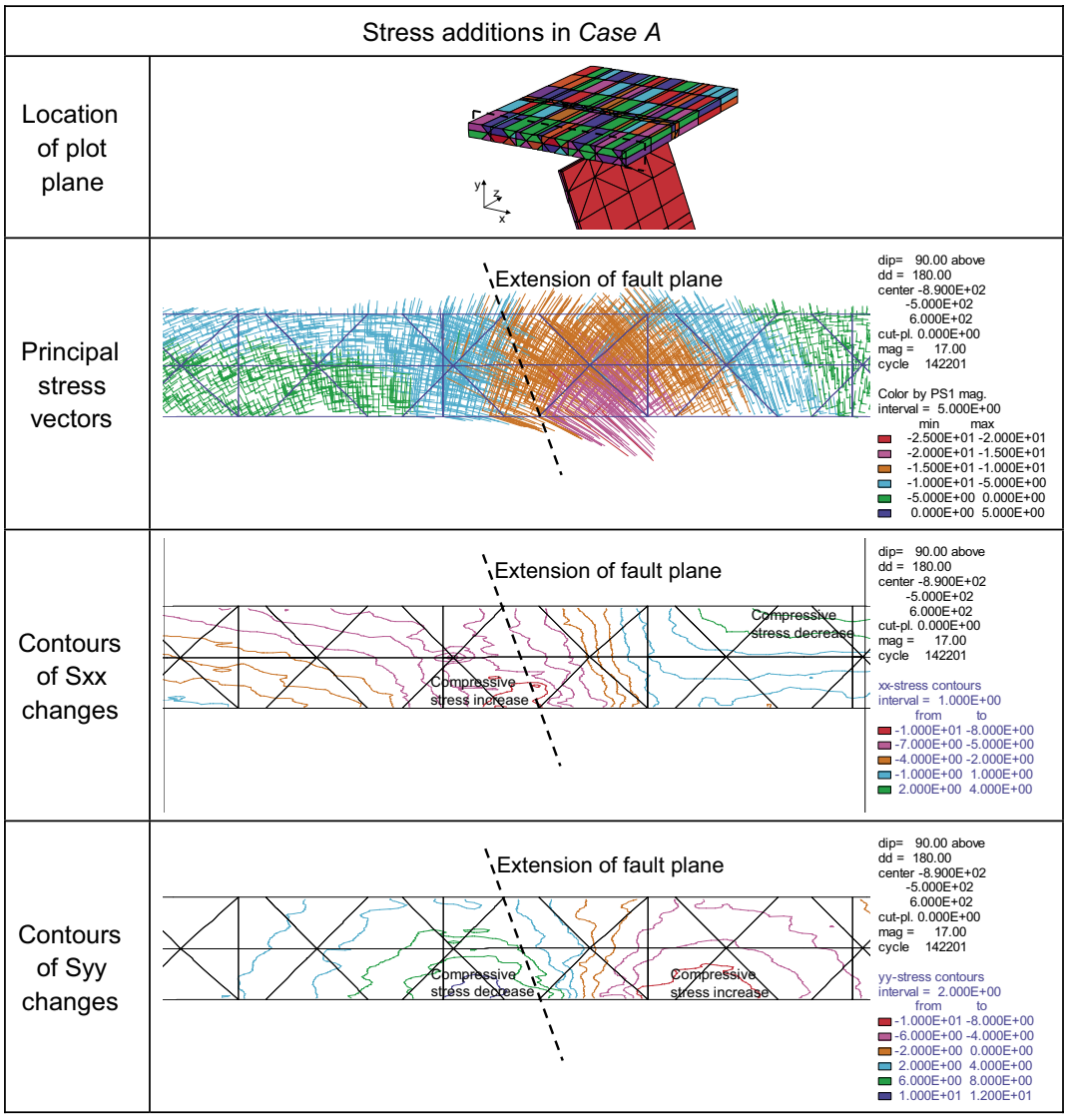

Figure 4-7. *Stress additions at 500 m depth in Case A calculated as the difference between the stresses at t = 10 s and at t = 0 s. The vertical section is located at z = 600 m, i.e. between the target fractures (upper). Positive values indicate compressive stress decrease (stress relaxation) and negative values compressive stress increase.*

The middle and bottom contour plots show stress changes in the x- and y-directions, respectively. Both compressive stress increase and stress decrease can be observed. In the x-direction, the stress increase amounts to about 9 MPa and the stress decrease to about 3 MPa. In the y-direction, the maximum stress increase amounts to about 8 MPa and the maximum stress decrease to about 10 MPa.

The deformation mode found in *Case B* results in less complicated stress redistribution (Figure 4-8). The horizontal compressive stresses oriented perpendicularly to the fault strike (x-direction) are decreased (positive stress additions). The maximum stress decrease amounts to about 14 MPa. This can be seen both in the principal stress vector plot (upper) and in the Sxx-contour plot (middle). In the vertical direction, there are minor stress changes of a few MPa (bottom).

As expected, the stress results show a much more extensive relaxation of the horizontal stresses in *Case B* than in *Case A*. In *Case B,* the compressive stress decrease amounts to about 14 MPa whereas the decrease is about 3 MPa in *Case A*.

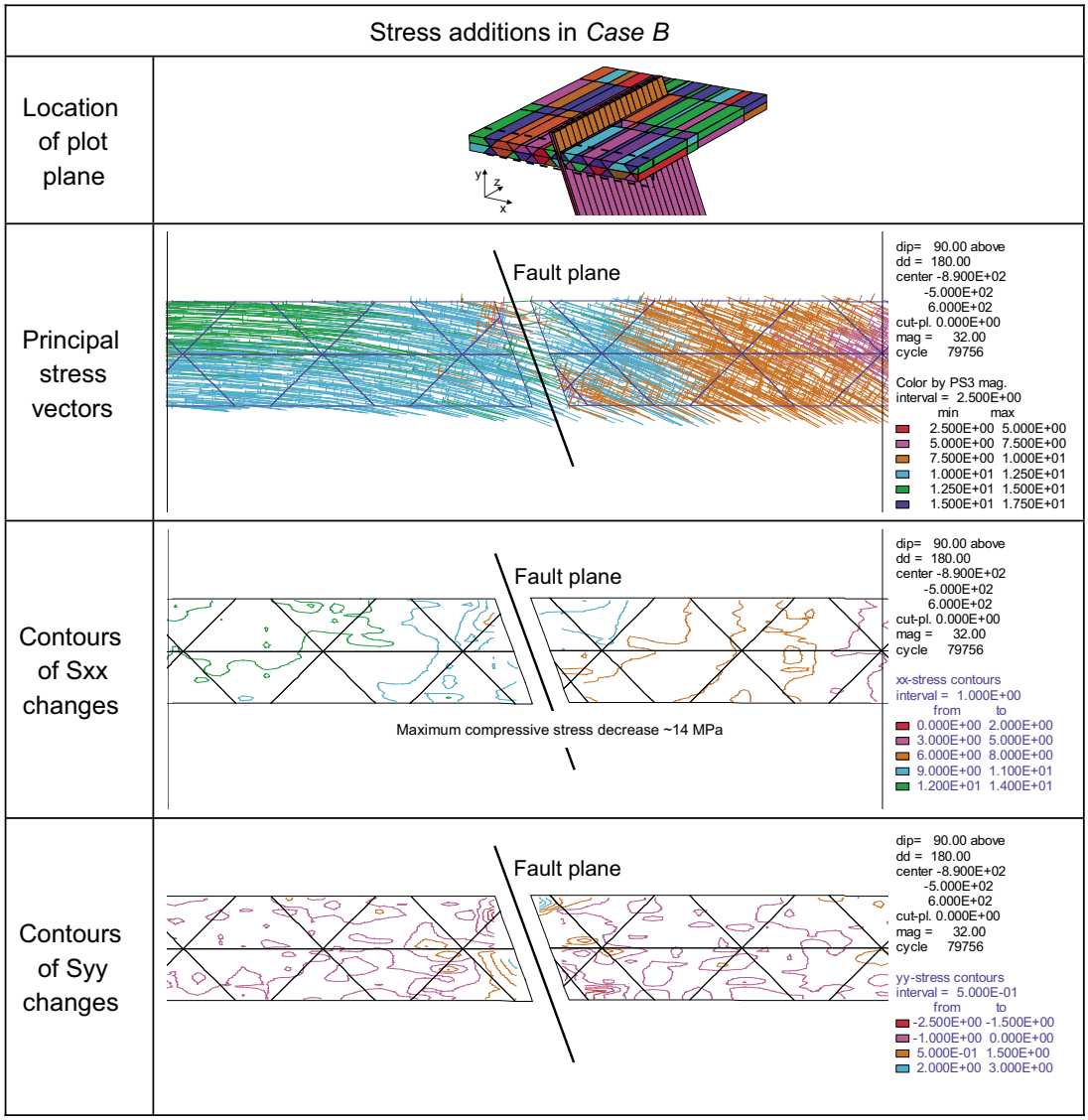

Figure 4-8. *Stress additions at 500 m depth in Case B calculated as the difference between the stresses at t = 10 s and at t = 0 s. The vertical section is located at z = 600 m, i.e. between the target fractures (upper). Positive values indicate compressive stress decrease (stress relaxation) and negative values indicate compressive stress increase.*

4.3 Target fracture stability analysis

The difference between the cases becomes clear when the stress states at 200 m distance from the primary fault are plotted in a Mohr's circle diagram (see Figure 4-9). The dotted line is the failure envelope for fractures with friction angle 34° and cohesion 0.5 MPa. The black semi-circle, which represents the initial stress state, indicates that the fractures are in a stable state before the earthquake, irrespective of dip.

After the earthquake, the major principal stress at the footwall side in *Case A* has increased and the minor principal stress has decreased such that the shear stress exceeds the stability limit for fractures within a 50 degree dip range. At the hanging wall side all fractures are stable also after the earthquake.

The stress states found in *Case B* after completed rupture indicate that the fractures are more stable after the earthquake than before. This is a logical result since the fault movement in that case results in an extensive relaxation of the horizontal stresses and thus reduced stress anisotropy.

Figure 4-9 shows the static equilibrium stress states before and after the earthquake. However, there are also dynamic stresses during the earthquake. These influence the target fracture strength and thus have importance for the amount of induced target fracture slip. Figure 4-10 shows the shear- and effective normal stresses on a 45° dipping plane located 200 m from the fault in *Case B*. The stresses were recorded at a point located between two target fractures (i.e. no slip permitted at this point). Along with the stress curves there is also a curve that shows the shear strength variation for a hypothetical fracture at that location. The shear strength is a function of the normal stress and was calculated as $c + \sigma_n * \tan(\alpha) = 0.5 + \sigma_n * \tan(34°)$. The following can be observed:

- The stability margin is larger after the earthquake than before. This is in line with the results shown in Figure 4-9.

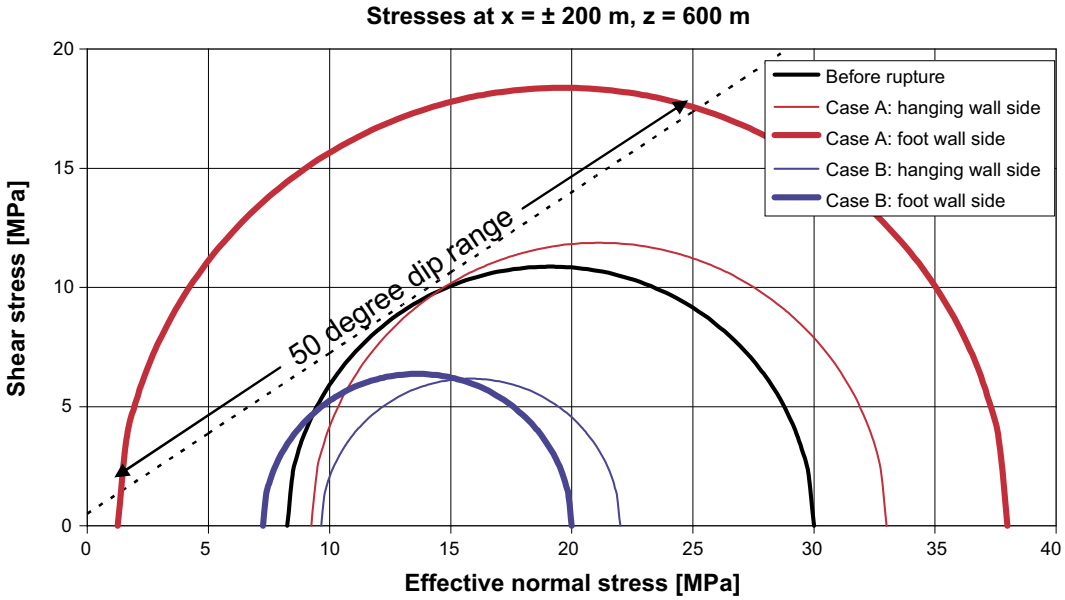

Figure 4-9. *Diagram with Mohr's circles illustrating the stress states at 200 m distance from the primary fault before and after the earthquake. The dotted line is the failure envelope for fractures with 34° friction angle and 0.5 MPa cohesion.*

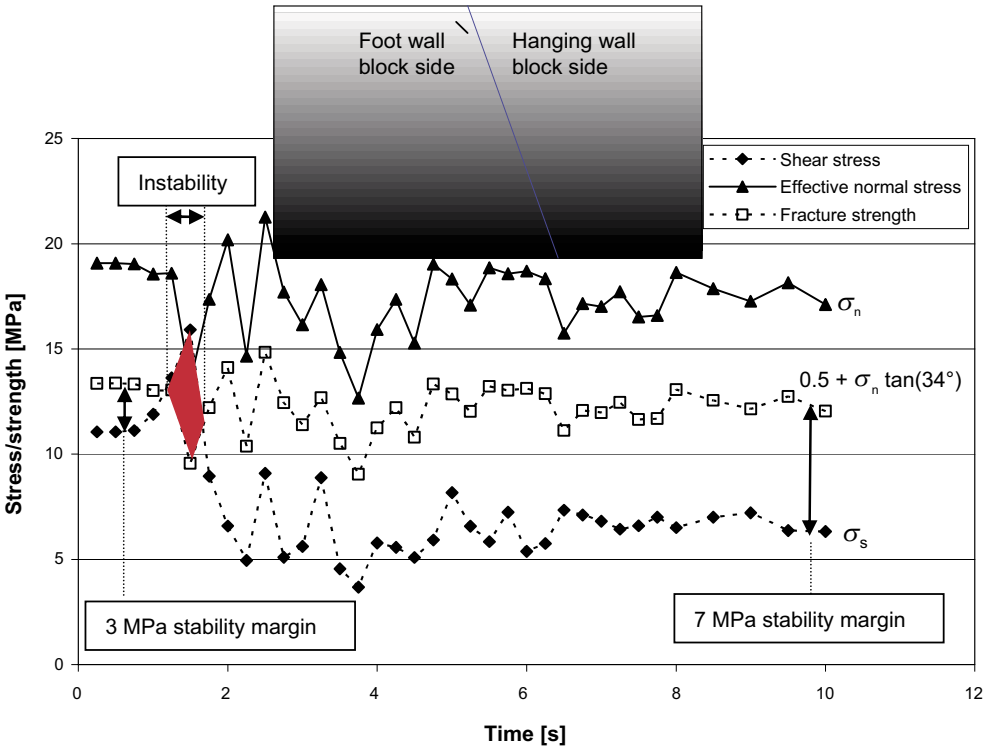

Figure 4-10. *Stress histories and corresponding shear strength of hypothetical footwall side fracture dipping 45° at a point 200 m from the primary fault.*

- Between 1.25 and 1.5 s after rupture initiation, there is an increase in shear stress and a simultaneous decrease in normal stress. The normal stress decrease yields shear strength decease and the shear strength drops below the acting shear stress for a little less than one half second. During that time a fracture at this location would slip. This indicates that dynamic stress oscillations have large importance for inducing target fracture slip, and that dynamic effects may trigger slip also in fractures that would be stable according to the static stress state. A static analysis would not capture slip occurring as result of such a temporary loss of strength.

4.4 Maximum induced slip on target fractures

The induced slip on target fractures is the key output parameter from the models. If the amount of induced slip on a target fracture that intersects a deposition hole is too large, it may damage the canister. According to SKB's canister damage criterion, fracture shear slip exceeding 100 mm across canisters count as canister damage /Hedin 2005/. The results here should be compared with that criterion.

Figure 4-11 shows an overview of the peak induced shear displacements of the target fractures in the two cases (A and B). Results from all fractures at 200 m and 600 m distance from the primary fault are shown. At larger distances, the displacements were small (all less than about 10 mm). The following can be observed:

- The largest slip (58 mm) was found in *Case B* on a target fracture with 270° dip direction, i.e. dip directed in the negative x-direction. The fracture was located close to the fault edge at 3600 m horizontal distance from the x-axis. The amount of slip was well below the canister damage criterion.

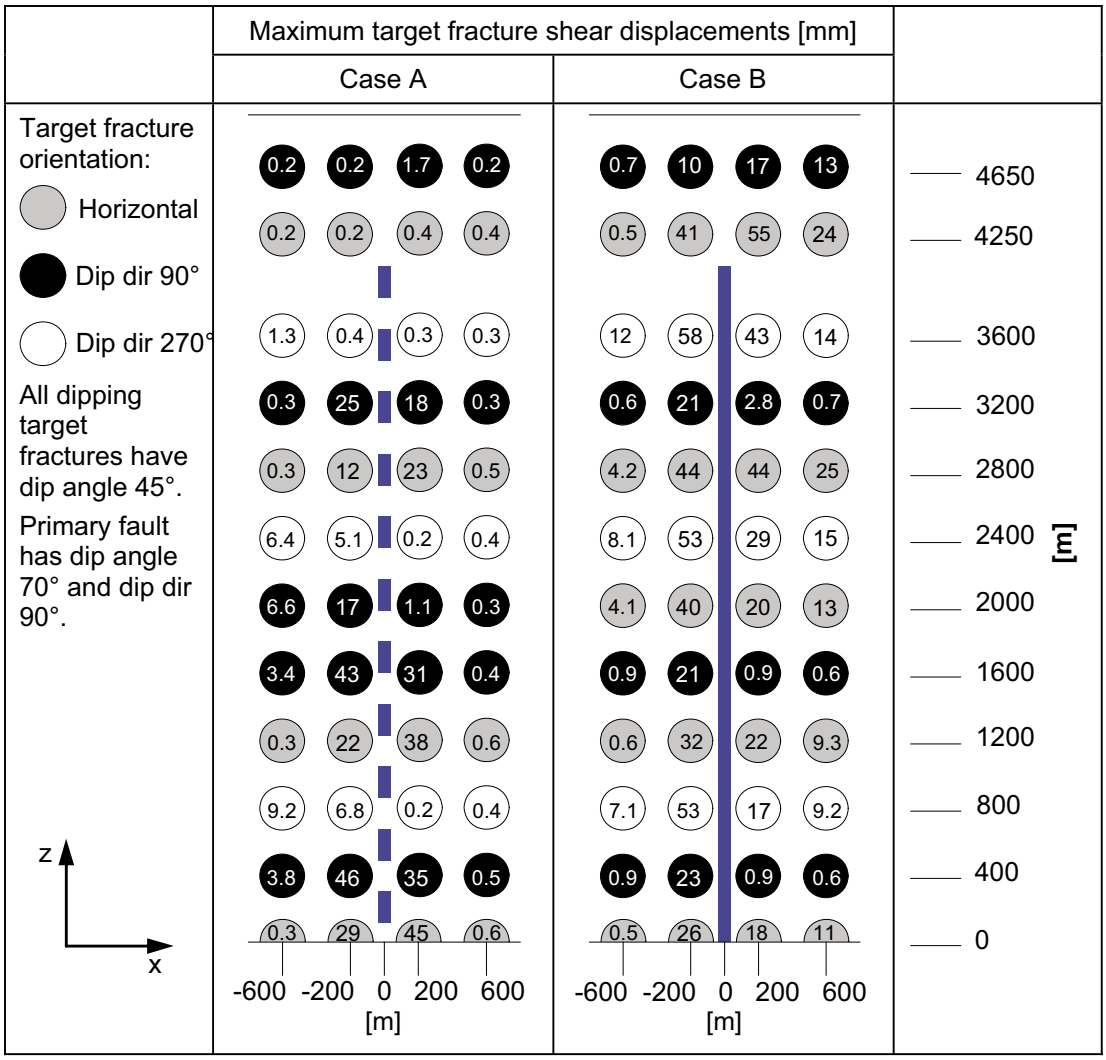

Figure 4-11. *Shear displacements for target fractures at 200 m and 600 m distance from the primary fault.*

- The fractures close to the faults vertical edge show larger slip in *Case B* than in *Case A*. This may be due to the stress concentrations around that edge. In *Case B,* fault edge effects influence the target fractures more than in *Case A* since the fault intersects the repository level in this case. In *Case A,* the edge's upper end is located 500 m below the target fractures.

Figure 4-12 shows vector plots of induced slip in the horizontal target fractures. The vectors are colored according to their amount of slip. The plots show the circular shapes of the target fractures. It can also be observed that fractures are affected at larger distances in *Case B* compared to *Case A* and that the shear directions are varied.

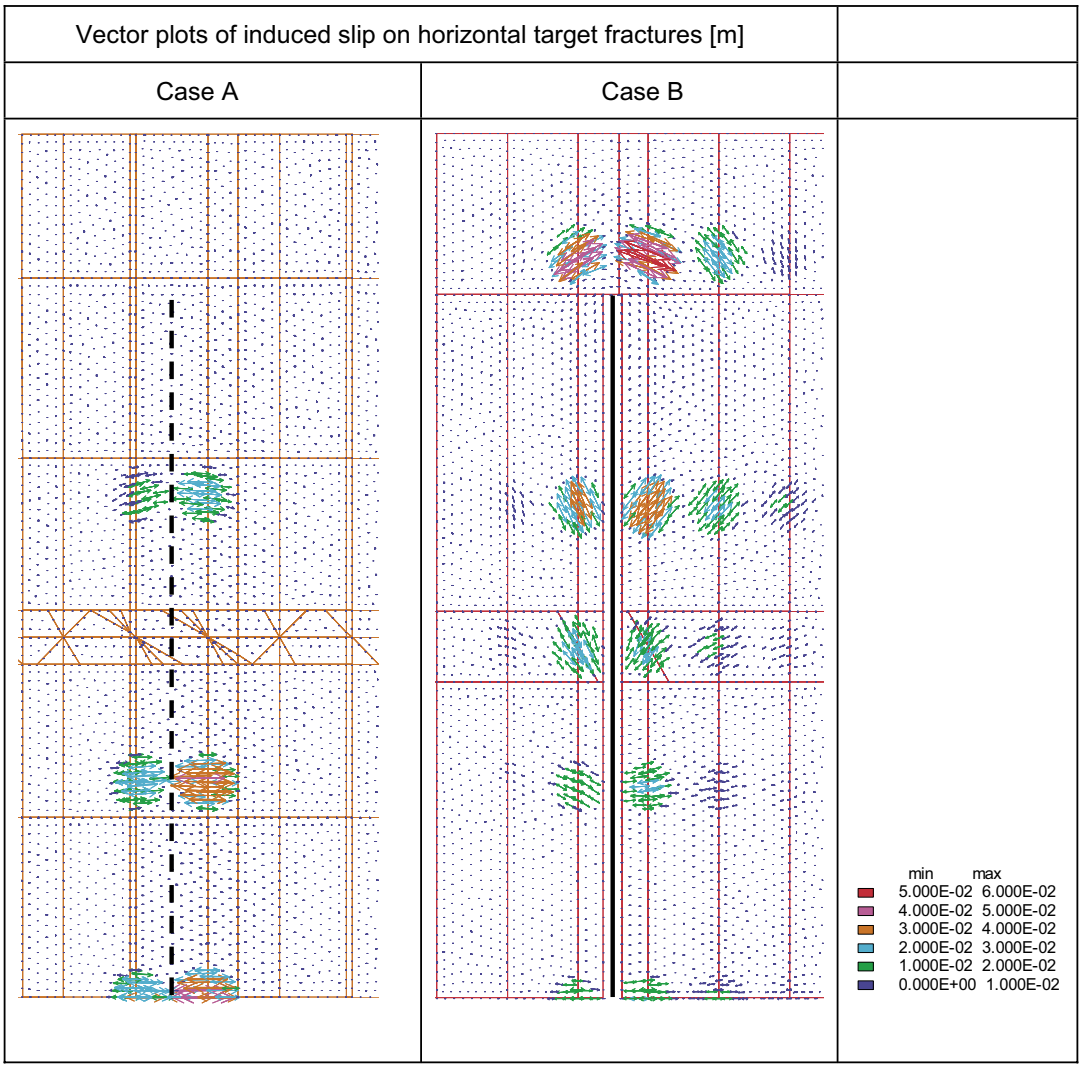

Figure 4-12. *Vector slip plots for the horizontal target fractures. The vectors are colored according to their magnitudes.*

Figure 4-13 shows the maximum and average target fracture slip for each fracture orientation as a function of distance. The following can be observed:

- The distance from the primary fault has a large importance for the amount of induced target fracture slip. In *Case A,* the average slip for all fractures at 200 m is about 16.5 mm whereas it is about 1.6 mm at 600 m distance. The corresponding results from *Case B* are 29 mm and 7.3 mm, respectively. At 1,000 m distance, the average slip was even smaller.
- Both the maximum and the average slip for a given type of target fracture differs between the two cases.

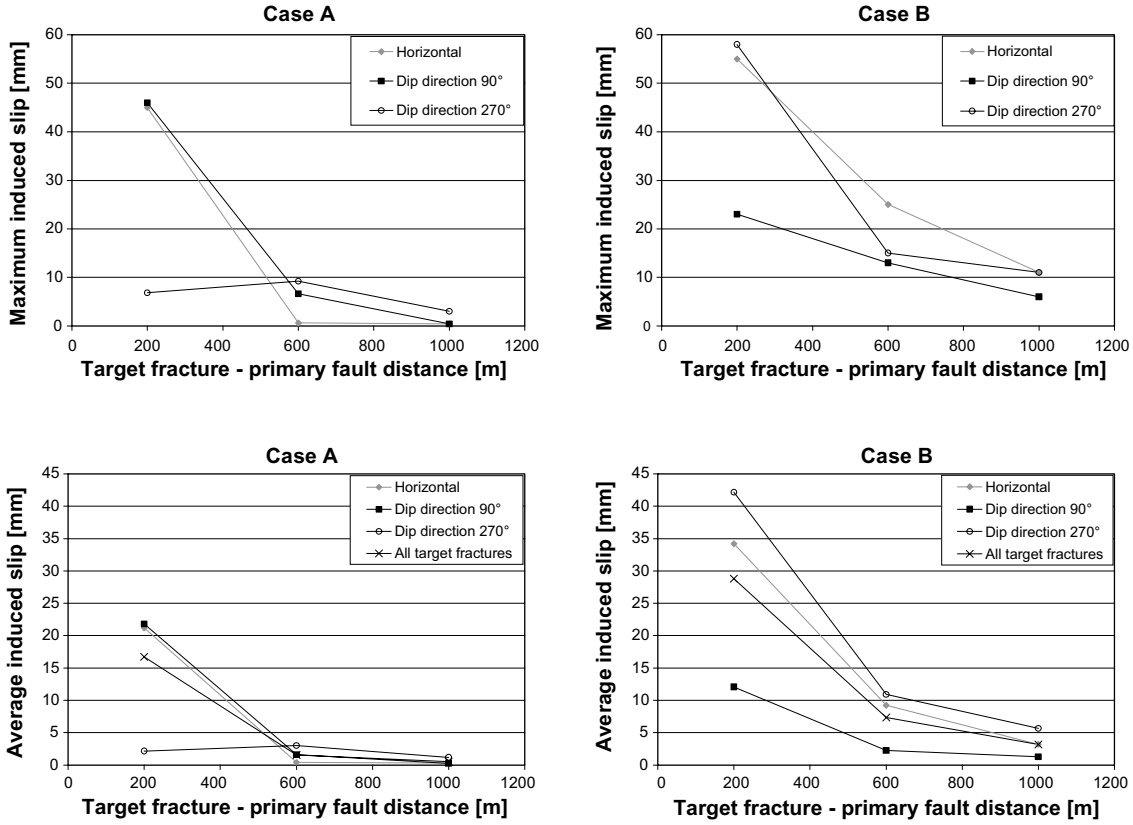

Figure 4-13. *Upper: Maximum target fracture induced slip at various horizontal distances from primary fault for Case A (left) and Case B (right). Lower: Average target fracture induced slip at various horizontal distances from primary fault for Case A (left) and Case B (right).*

4.5 Time development of target fracture slip

4.5.1 General

In the following sections, target fracture slip histories are presented. In Section, 4.5.2 results from the *Case A* model are presented and in Section 4.5.3 the *Case B* results are shown. Results from all target fractures are not included. For each horizontal distance (along x-axis) from the primary fault and fracture orientation, only results from the fracture that slipped most are shown. Results from the target fractures at 1,500 m distance from the primary fault are excluded since the slip in these fractures was found to be insignificant.

4.5.2 Case A: Buried rupture

The results in this section come from *Case A,* which is the type of event numerically analyzed in /Munier and Hökmark 2004/. The rupture's upper edge is located 1,000 m below the ground surface. With this geometry, the relaxation of shear stresses along the primary fault is accompanied by a stress concentration around the upper fault edge. This means that the rupture results in significant changes in the stress field in the region between the fault edge and the ground surface, i.e. in the region where the target fractures in the model are located (cf Section 4.2).

In Figures 4-14 to 4-16, target fracture slip histories are presented. In each figure, one target fracture orientation is considered. The following can be observed:

- All target fracture displacements are fully developed after about 2.5 seconds. This corresponds to the duration of the rupture (cf Figure 4-2, left).

- There are displacements on all fractures, also at the hanging wall side where the stress state after the earthquake is very similar to the initial stress state (cf Figure 4-9). No slip would have occurred if that stress change had taken place aseismically. This confirms what was concluded in Section 4.3; the dynamic effects are important for inducing target fracture slip.

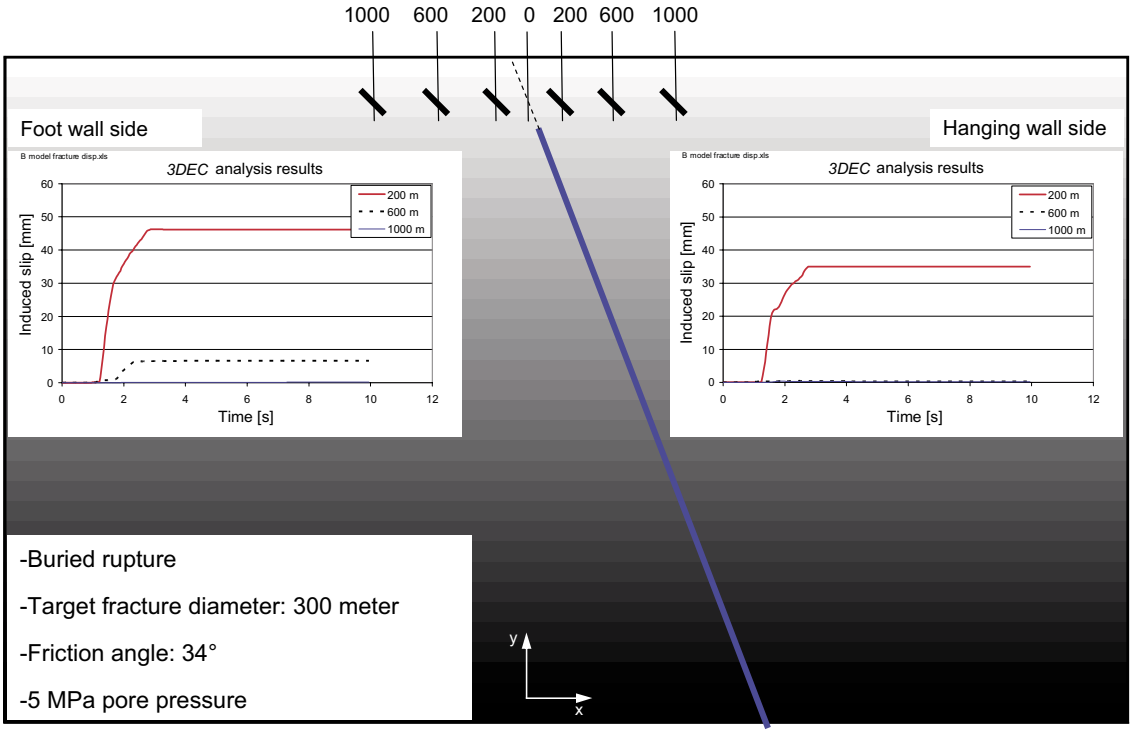

Figure 4-14. *Induced slip on Case A target fractures with dip direction 90°.*

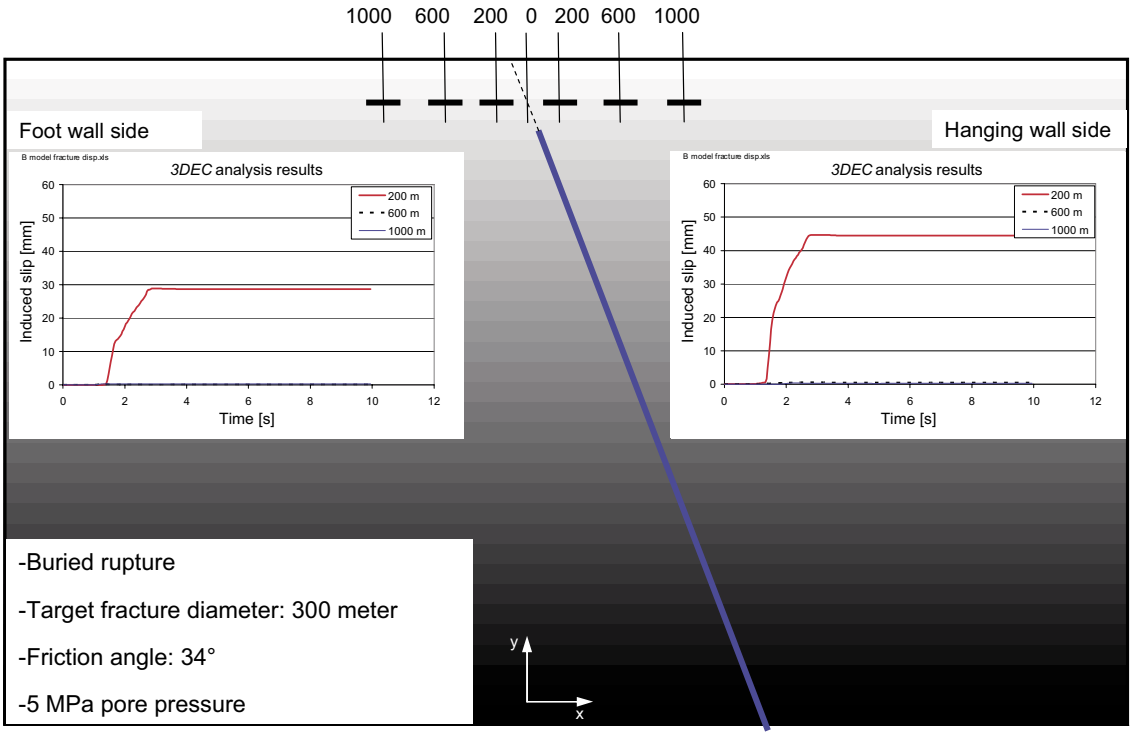

Figure 4-15. *Induced slip on horizontal Case A target fractures.*

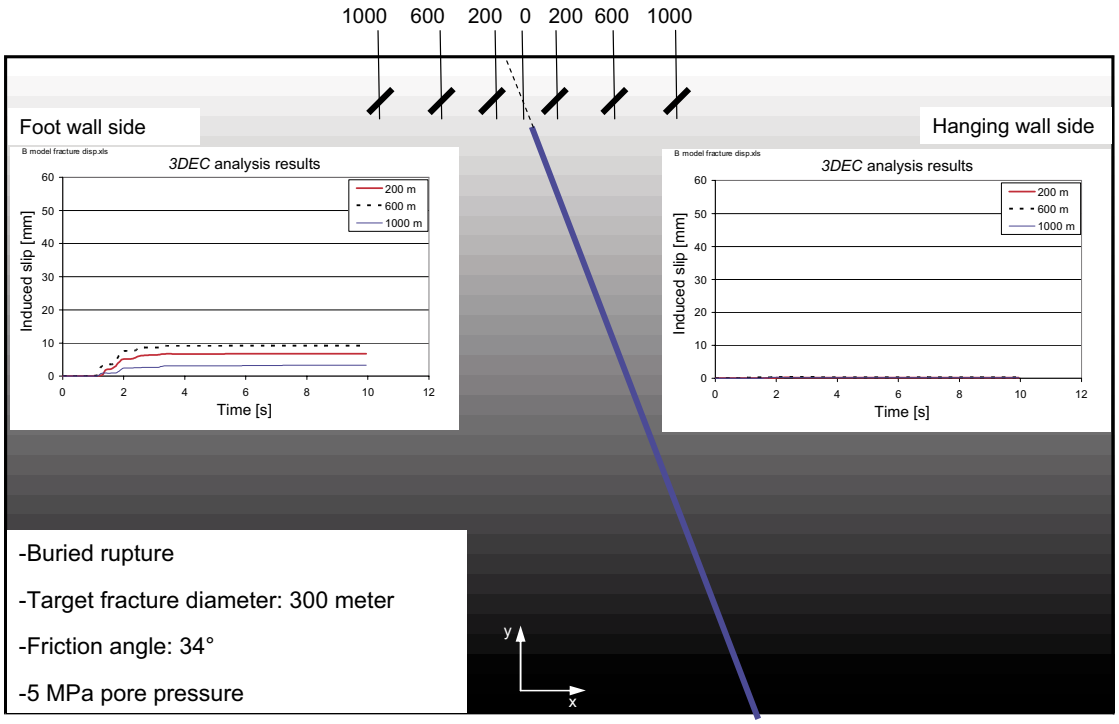

Figure 4-16. *Induced slip on Case A target fractures with dip direction 270°.*

4.5.3 Case B: Rupture breaching the ground surface

In Figures 4-17 to 4-20, the target fracture slip histories found in *Case B* are shown. In addition to the results from the fractures located at 200 m, 600 m and 1,000 m distance, there are also results from the target fracture that intersected the primary fault (Figure 4-20) (cf Figure 3-4, right). The curve that is shown regards the fracture at z = 0 which had the largest peak slip. The following can be observed:

- Target fractures on both sides of the fault slip, irrespective of dip and dip direction, although the net stability margin increases everywhere (cf Figure 4-9).
- For the footwall fractures shown in the Figure 4-17, the slip takes place during a period of about one half second. This period coincides with the period of loss of stability for these fractures (cf Figure 4-10).
- In the results from the horizontal fractures (Figure 4-18), some oscillations can be observed. All dipping fractures move in one direction only.
- All target fracture displacements are fully developed after about 3 seconds. This corresponds to the duration of the primary fault rupture (cf Figure 4-2, right). There is an exception for the fracture that intersects the primary fault (Figure 4-20).
- The maximum slip found on the target fracture that intersects the primary fault is 113 mm, i.e. above the 100 mm criterion (Figure 4-20). However, since this fracture intersects the primary fault, it is subjected to large and complicated loads. Contrary to the other target fractures, the displacement is not completed until after about 5 seconds. This is because the behavior of this fracture is directly influenced by the low strength primary fault which continues to oscillate after the rupture (cf Figure 4-2, right).

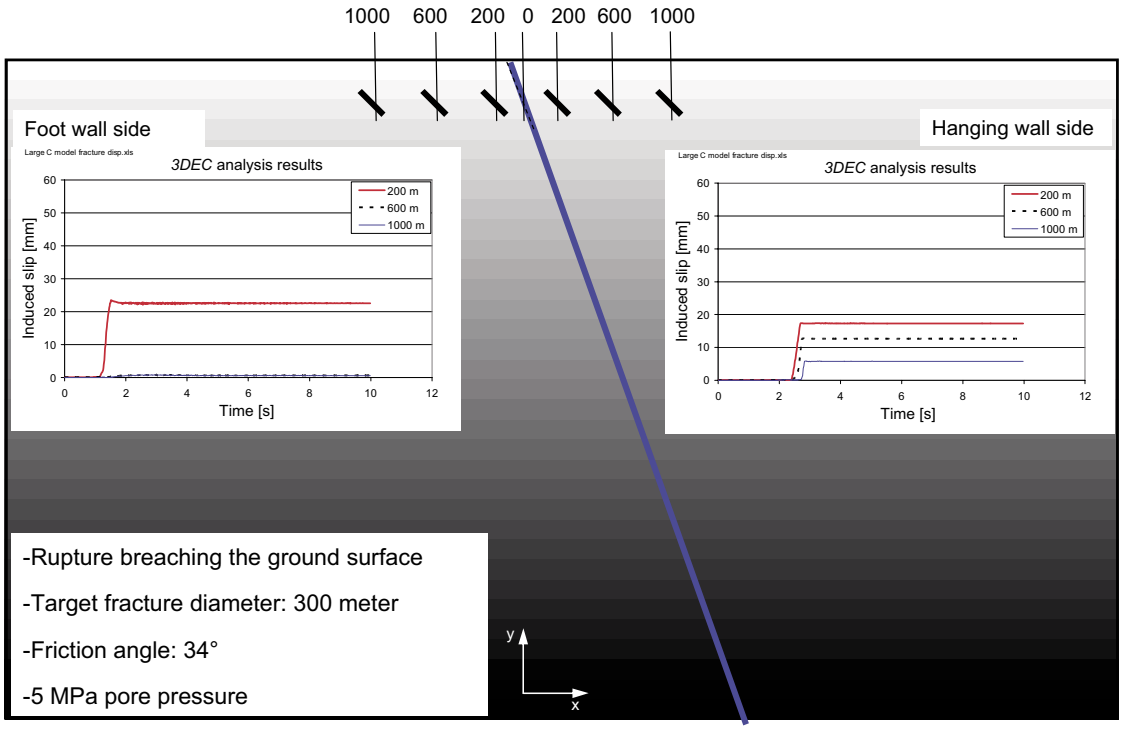

Figure 4-17. *Induced slip on Case B target fractures with dip direction 90°.*

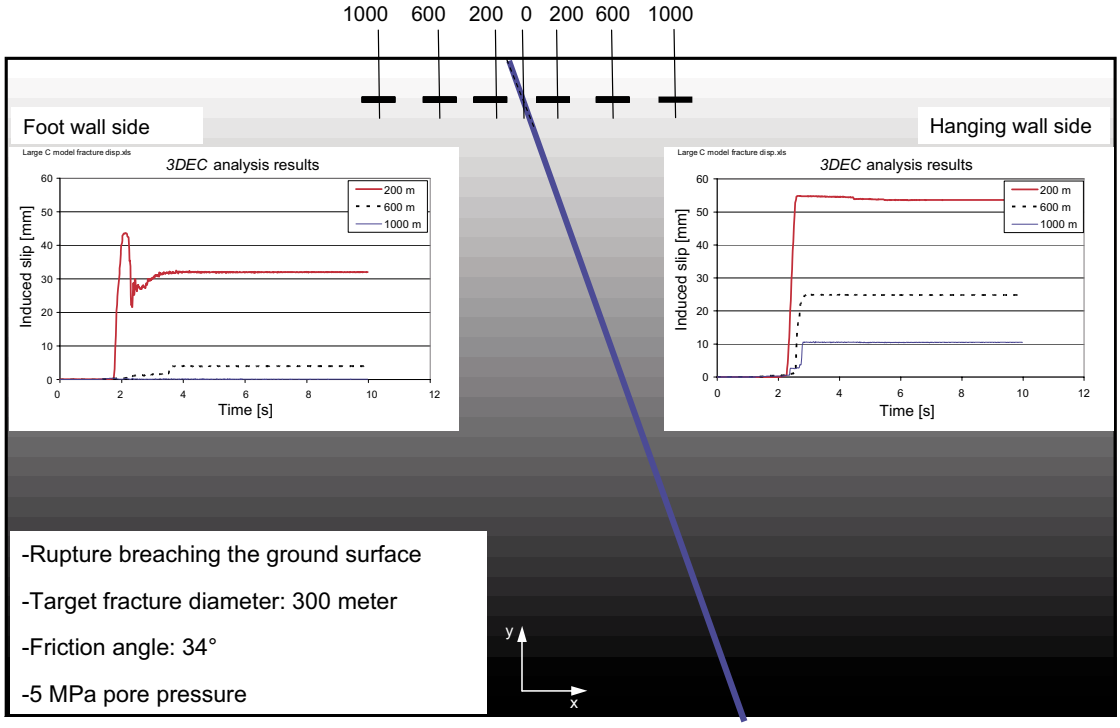

Figure 4-18. *Induced slip on horizontal Case B target fractures.*

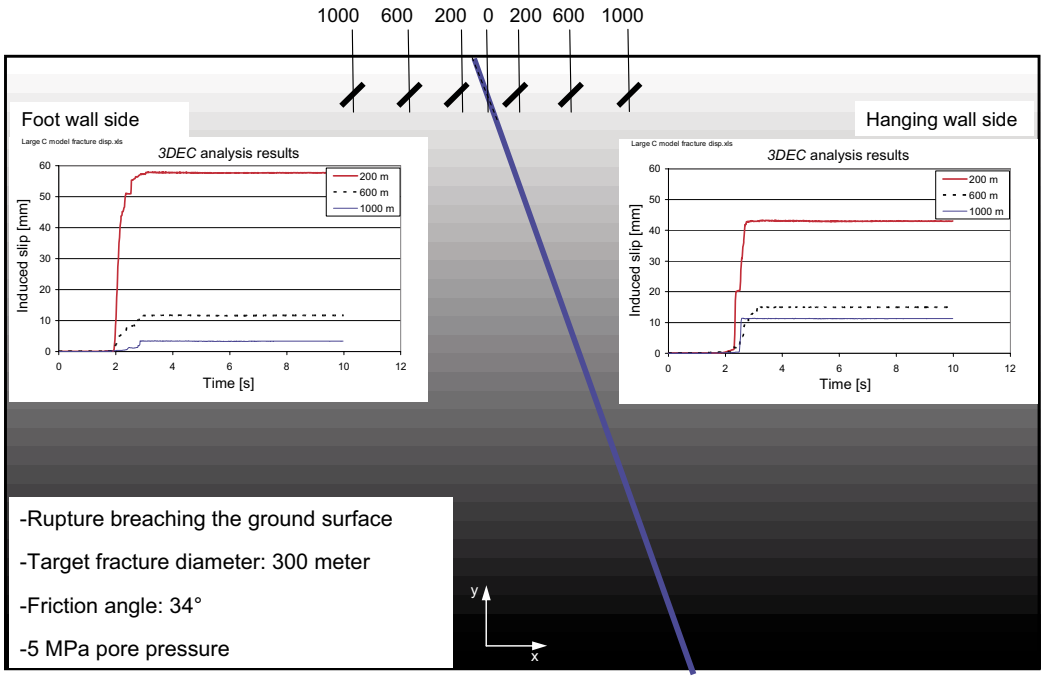

Figure 4-19. *Induced slip on Case B target fractures with dip direction 270°.*

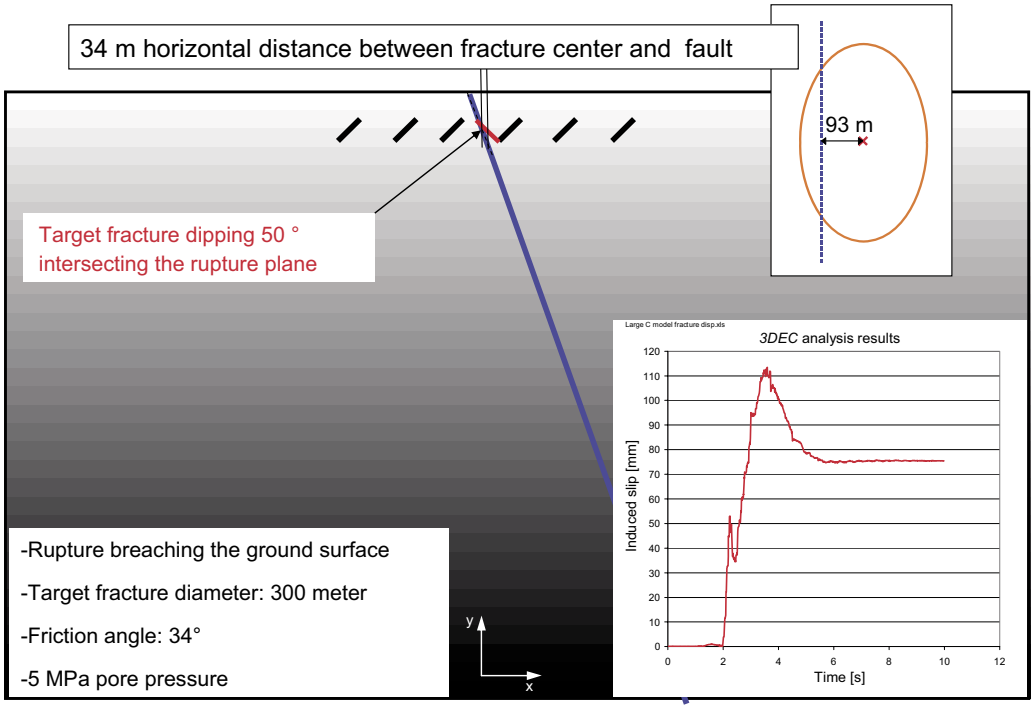

Figure 4-20. *Induced slip on Case B target fracture that intersects the primary fault.*

4.6 Induced slip velocities

The maximum slip velocities for the target fractures with the largest amount of induced slip (cf Section 4.5 above) are shown in Figure 4-21. The velocity histories for the fractures with the highest velocities are shown in Figure 4-22. The velocities are in general higher in *Case B* compared to *Case A*. The maximum target fracture slip velocity in *Case* A is 109 mm/s whereas the maximum velocity in *Case B* is 862 mm/s, i.e. about eight times higher.

Fracture slip velocities are not regular output from *3DEC*. The velocities had to be derived from the target fracture slip histories presented in Section 4.5. Thus, there is some influence on the results of the sampling frequency used when the displacement histories were recorded. It also turned out that the velocities are sensitive to details in the finite difference element mesh. This gives uncertainties in the velocity results and the maximum velocities may vary within ± 50%.

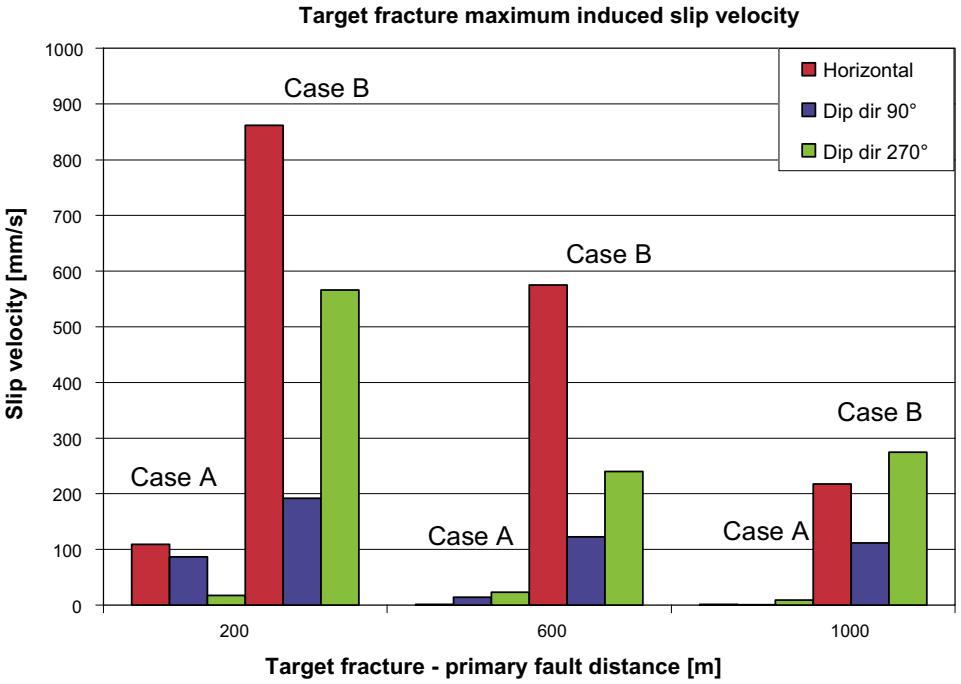

Figure 4-21. *Maximum slip velocities found among the target fractures.*

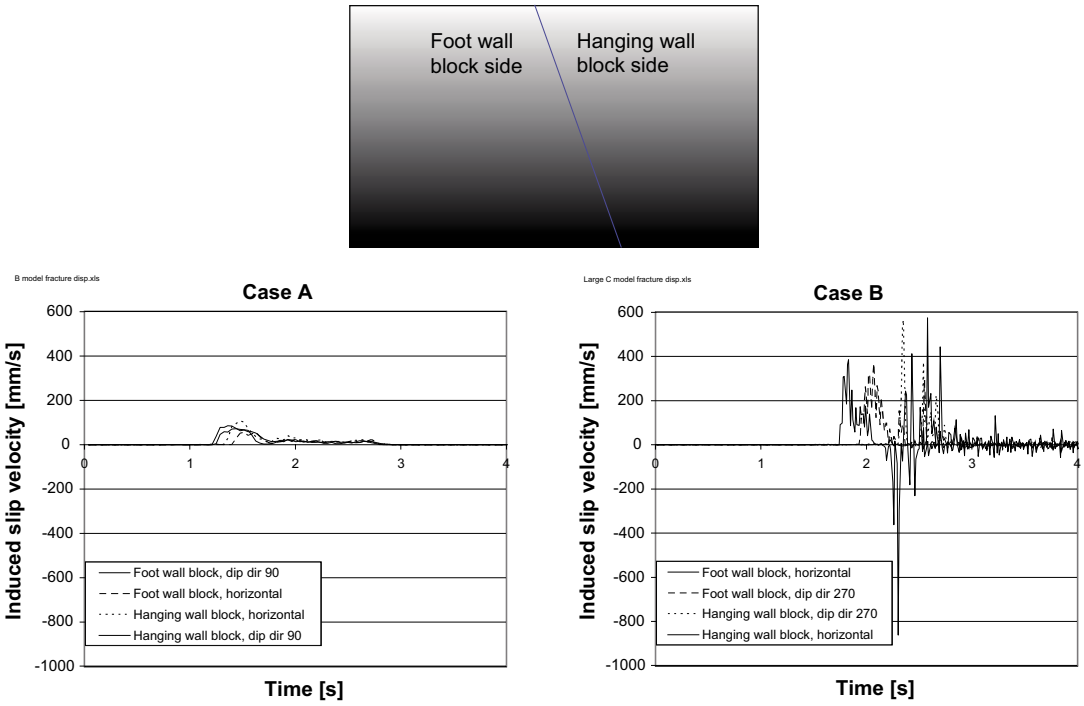

Figure 4-22. *Induced slip velocities during the first four seconds. The target fractures have in general higher slip velocities in Case B than in Case A.*

5 Relevance and validity

5.1 General

In this chapter, the relevance and validity of the modeling approach are considered. Results are compared with results from a similar model analyzed in a previous study. Besides this, the limitations and the conservatism in the modeling approach are discussed.

5.2 Benchmarking

In the *Case A*-model, there was a frictionless target fracture located at 2,000 m horizontal distance from the upper edge of the primary fault (cf Figure 3-4, left). The shear displacement of this fracture was compared with corresponding results from the step 3 *FLAC3D* simulation /Munier and Hökmark 2004/. The target fracture in that model was square-shaped with an edge half-length of 100 m whereas the fracture in *Case A* had a radius of 150 m. It can be shown with closed-form solutions that the maximum fracture shear slip depends linearly on the fracture length /Pollard and Segall 1987/. Therefore, the results from the *Case A*-fracture were multiplied with the factor 2/3 to be comparable with the *FLAC3D* results. Since it is mainly the fracture length in the shear direction that controls the amount of slip, the results can be compared even though the shapes of the fractures were different.

The results from the two models are shown in Figure 5-1. The agreement between the results is good. The response comes after about one second in both models and the maximum displacement is almost equal. The residual displacement is about 0.5 mm larger in the *Case A*-model than in the *FLAC3D* model. The differences may arise from differences in zoning and damping settings. Contrary to the target fractures at 200 m, 600 m and 1,000 m distance, this particular benchmark fracture is frictionless. This means that there are no locked-in stresses and that the fracture slips immediately when subjected to arbitrarily small shear loads. This explains the long time of small oscillations.

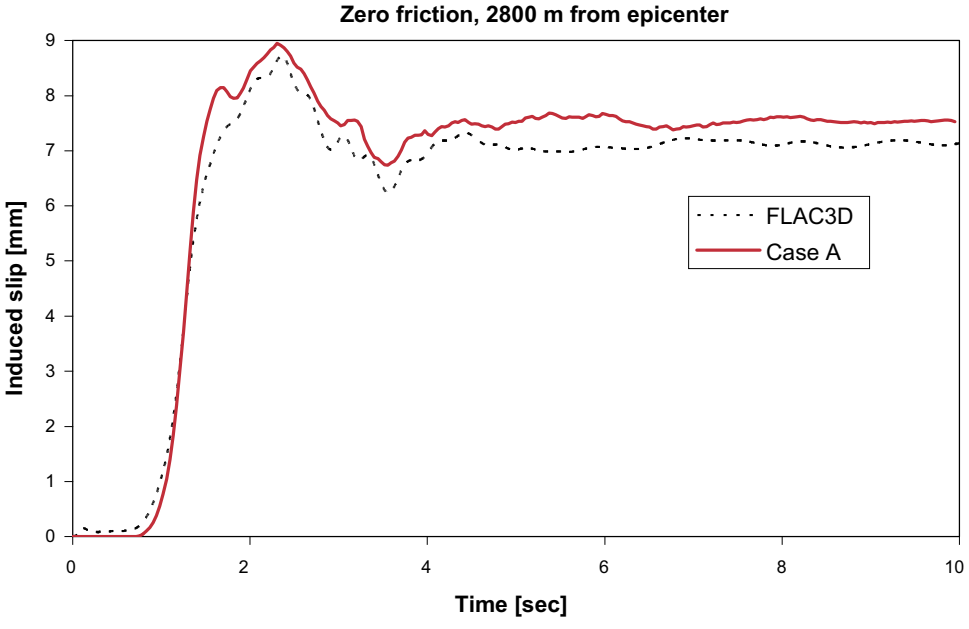

Figure 5-1. *Induced shear slip on a frictionless target fracture at 2,800 m horizontal distance from epicenter. Comparison between previous FLAC3D simulation and Case A.*

5.3 Rupture area, primary fault slip and stress drop

The magnitude scale used here is based on the seismic moment. It is the product of the primary rupture area, the average primary slip and the rock mass shear modulus (cf Equation 1-3). The relations between these three factors means that an event of given moment magnitude may be modeled using a small slip combined with a large rupture area or vice versa (cf Equation 1-3). Figure 5-2 shows database regressions by /Wells and Coppersmith 1994/ of the correlation between earthquake magnitude and rupture area. In the figure, the resulting magnitude and rupture area for the *Case A* model is indicated. The figure shows that the rupture area in the model is within the bounds of the data from the database (left) but is about half the area suggested by the regression line for reverse type events (right). Thus, the average slip in the model must be relatively large. This is also what can be observed in Figure 5-3, which shows the correlation between the average slip and magnitude based on database data. The average primary slip in the *Case A* model is significantly larger than the average for magnitude 6 events.

Figure 5-4 shows an example of a stress drop distribution found in a study of the Uemachi fault system in Japan /Sekiguchi et al. 2004/ This distribution may be regarded as realistic (or rather less idealized than the schematic stress drop distributions assumed here). When the distribution and the amount of stress drop in the figure are compared with those used in this study, the following observations can be made:

- The figure shows a much more heterogeneous stress drop distribution compared with the ones used in the present study. The stress drop distribution in the present study models was idealized and was only varied with depth (cf Figure 3-8). However, for the purpose of the present work, the idealized distribution that was used here is judged to be relevant.
- Near the surface, for down-dip distances between 0 and 5 km, the stress drop shown in the figure is typically below 5 MPa. In the models analyzed here (rupture reaching depth of about 5 km), the average stress drop was about 15 MPa. A higher stress drop yields more extensive stress redistribution around the fault which results in a larger impact on the target fractures.

From the discussion above it can be concluded that in the earthquake simulations performed here, relatively small rupture areas were used along with relatively large primary fault shear slip. If the *3DEC* model had been dimensioned to fit the regressions shown in Figure 5-2 and 5-3, for instance, the induced target fracture slip would have been significantly smaller.

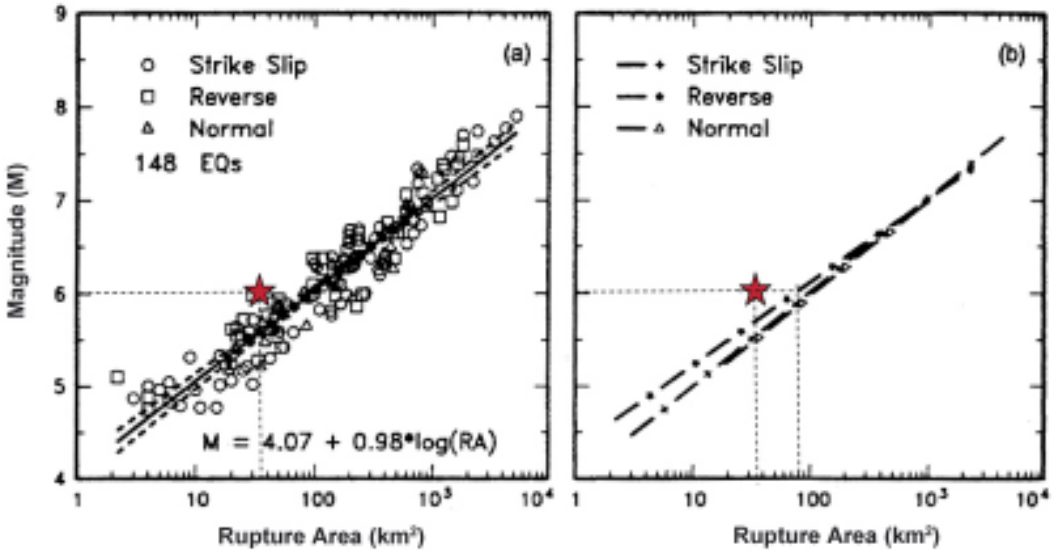

Figure 5-2. *Comparison between results from the Case A model and database regression of the correlation between earthquake magnitude and rupture area. From /Wells and Coppersmith 1994/. The rupture area in the Case A model is indicated in the figure.*

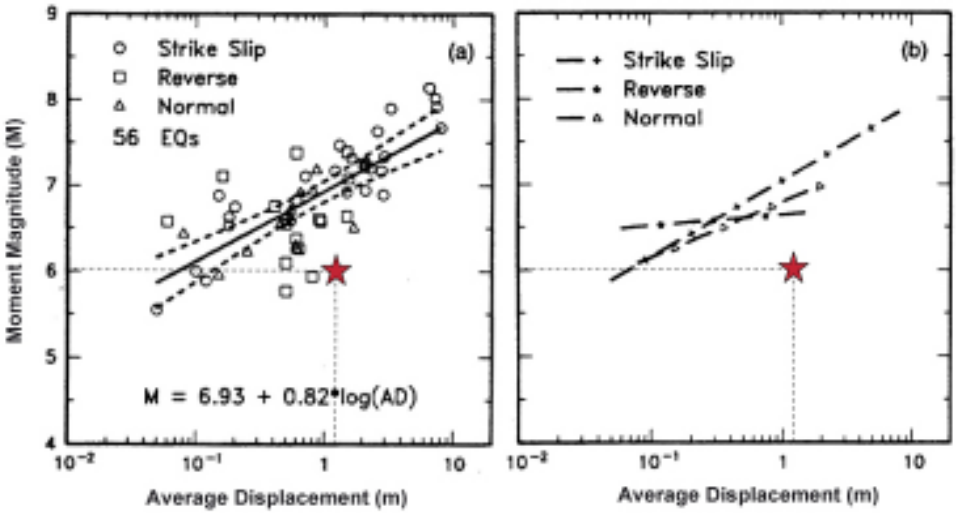

Figure 5-3. *Database regression of the correlation between earthquake magnitude and average fault slip. From /Wells and Coppersmith 1994/. The average primary fault slip in the Case A model is indicated in the figure.*

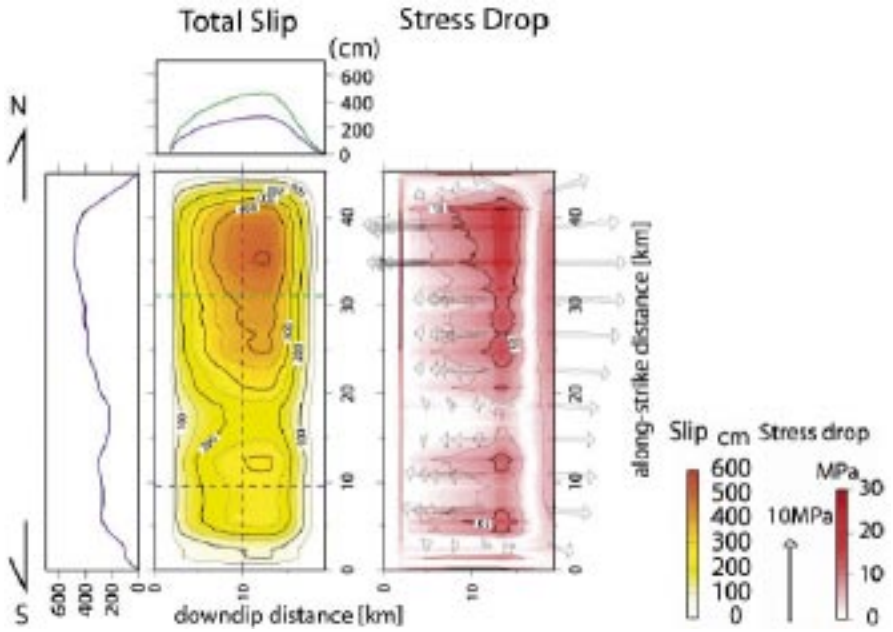

Figure 5-4. *Static slip model and static stress drop model for the Uemachi fault system. From /Sekiguchi et al. 2004/.*

5.4 Primary fault shear velocity

The results in this work indicate that the dynamic effects are of great importance for the amount of induced target fracture slip. The stress oscillations in the models are induced by the rupture process in the primary fault and by the accompanying primary fault slip. The diagram in Figure 5-5 shows the fault shear velocity found close to the ground surface in *Case B*. The maximum velocity is 3.8 m/s. This value can be compared with maximum shear velocities reported from real events. The 1999 Chi-Chi earthquake (M7.6) displayed a maximum shear velocity of roughly 2.5 m/s near the surface /Ma et al. 2003/ and for the Landers earthquake (M7.2), the maximum velocity was estimated to 1.5 m/s /Wald and Heaton 1994/. Thus, the primary slip velocity found in the model described here is about twice as high as in those observations. Stress wave amplitudes scale with the particle velocity amplitudes /see e.g.

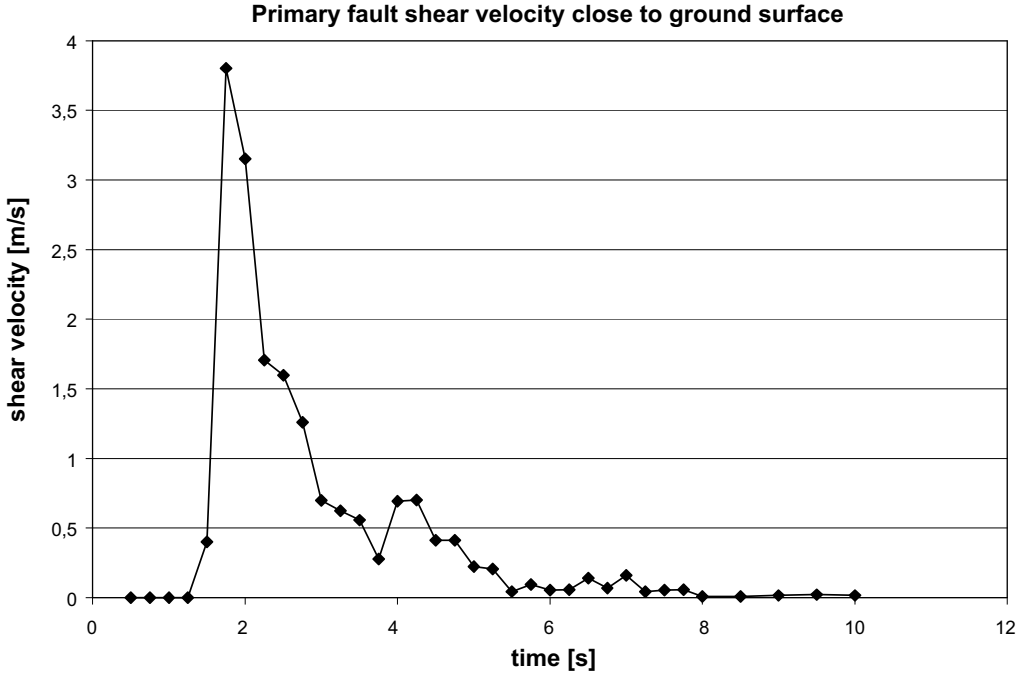

Figure 5-5. *Primary fault shear velocity close to the ground surface in Case B.*

Itasca 2003/. This means that the overestimated shear velocities (and particle velocities) give correspondingly overestimated stress wave amplitudes. A 50% reduction of the primary fault shear velocity in the model would give corresponding reductions of the stress wave amplitudes and much less impact on the target fractures (cf Figure 4-10). It can be concluded that the magnitudes of the stress waves in the models are over-predicted rather than under-predicted.

5.5 Target fracture shear strength

5.5.1 Shear rate

The target fractures were assumed to have shear strength according to a Coulomb criterion with values of friction angle and cohesion derived from site data /Fälth and Hökmark 2006/. The data regard fractures subjected to static loading and does not account for any shear velocity dependence. There are test results in the literature that indicate that rate dependence of fracture shear strength may be a possibility. Figure 5-6 shows laboratory test results from /Barbero et al. 1996/. The figure shows the ratio between dynamic and static shear stress for three different materials and for two different normal stress levels. It is difficult to translate the laboratory test results to the conditions at depth under seismic loading, but they point to the possibility that the dynamic shear strength may be different from the static one. This issue remains to be addressed in future studies.

5.5.2 Fracture size and geometry

As noted above, the target fracture shear strength parameter values were derived from site data. This data was obtained from tests with typical test sample sizes, i.e. in the order of 0.1 m, whereas the target fractures in the models here have radii of 150 m. In addition, all target fractures were assumed to be perfectly planar and continuous without kinks or large-scale rough irregularities. These assumptions imply that the effective fracture size (length in slip direction) may be overestimated here. From the modeling point of view, as far as the average fracture slip is concerned, this is equivalent to underestimating the fracture shear strength.

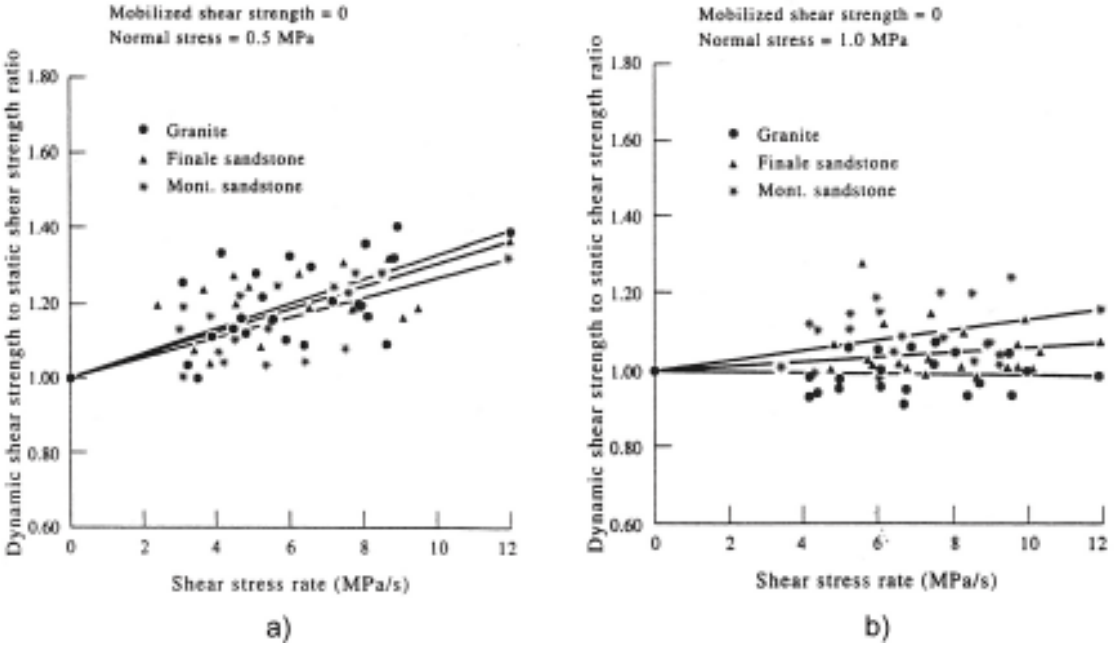

Figure 5-6. *Rate dependence in shear resistance for granite and sandstones. Dynamic shear strength to static shear strength ratio vs. shear stress rate. a) normal stress 0.5 MPa and b) normal stress 1 MPa. From /Barbero et al. 1996/.*

5.6 Fracture population

To make an estimate of the amount of energy that is released during an earthquake and which could be expended on target fracture slip is a complicated matter. Here it is just concluded that if estimates of possible fracture slip based on available strain energy should be attempted, the energy would have to be distributed on a certain amount of fracture area. The fracture area per unit of modeled rock mass volume is small compared with what is found in real rock masses. In the models, the specific fracture area is of the order of 0.02 m^2/m^3 in the repository region, whereas it is estimated to be in the range of 3–15 m^2/m^3 at the candidate sites /La Pointe et al. 2005, Hermanson et al. 2005/. Therefore, it can be concluded that the amount of released energy per unit target fracture area in the models is high, which is conservative.

5.7 Fracture propagation

In the models analyzed here, the rock was assumed to behave elastically and no effects of fracturing of the rock around the tips of slipping target fractures were considered. /La Pointe et al. 2000/ made an attempt to quantify such effects. However, in that study the fracture propagation criterion was schematic and approximate, and the propagation process was not coupled with the associated change in fracture size. The propagation will give changes in the stress field and in the fracture geometry. Here it is just concluded that in the present models, no energy was expended on fracture propagation. Similar to the previous point, this may mean that the amount of energy available for shear slip on the individual fracture has been overestimated. The effects are difficult to quantify and may have to be addressed in future studies.

6 Conclusions and discussion

6.1 General

The results presented in this report relate to the risk of canister damage in the deep repository due to future glacially induced earthquakes. The main objective of the work was to assess the effects on rock fractures at repository depth of a large glacially induced earthquake in a nearby pre-existing fault. This was done by numerical modeling with the distinct element code *3DEC*. The modeling approach allowed the study of the combined effects of the static process (stress redistribution around the fault) and dynamic processes (propagation of stress waves).

The earthquake was assumed to originate on a steeply dipping fault striking perpendicularly to the major in situ stress. The major horizontal in situ stress was set sufficiently high to power a magnitude 6 dip-slip earthquake on a rupture area of about 40 km^2. The rupture was initiated at the hypocenter some 3 km below ground surface and programmed to propagate along the fault plane with a given rupture propagation velocity and with a schematic but reasonably realistic representation of the failure mechanism. Two cases of fault geometry were analyzed: one with a buried rupture (*Case A*) and one with the rupture breaching the ground surface (*Case B*).

Numerous circular target fractures, all with 150 m radius and with different orientations were modeled. The target fractures were located at 500 m depth and at distances between 200 m and 1,500 m from the fault. The target fractures had shear strength properties according to Forsmark and Laxemar site data. A constant 5 MPa pore pressure was specified for all target fractures. No attempts were made to assess effects of possible pore pressure transients. The focus of the report is on the behavior of the target fractures, in particular on whether the target fracture slip would exceed the present-day canister damage criterion (100 mm).

6.2 Target fracture slip velocities

The maximum target fracture slip velocity found in *Case A* was 109 mm/s whereas the maximum velocity in *Case B* was 862 mm/s. These velocities are considerably higher than those presented in earlier studies. Figure 6-1 shows shear velocities calculated with the WAVE code /Munier and Hökmark 2004/. The maximum WAVE slip velocity is about 80 mm/s. The large differences between the WAVE results and the present *3DEC* results can be explained by the difference in target fracture mechanical properties. In the WAVE model, the target fractures were frictionless. Every change in shear load causes the fracture to displace such that no strain energy is accumulated. This gives continuous and slow deformations. A different situation arises when the fractures have friction. All target fractures in *Case A* and *Case B* have a 34° friction angle. Due to the shear strength, strain energy accumulates during loading. When the shear strength is exceeded after a few seconds of loading, the fracture slips and the accumulated energy is suddenly released, giving high slip velocities.

The maximum slip velocity of 862 mm/s calculated here should be compared with the shear velocity assumed in earthquake analyses of the buffer/canister system. /Börgesson et al. 2004/ assumed the shear velocity to be 1,000 mm/s at maximum. Since the stiffness of the bentonite surrounding and protecting the canister is strain rate dependent, i.e. increases with increasing rate, the maximum target fracture slip found here would result in less load on the canister than in the worst case simulated in that study. The sensitivity of the canister/buffer system to shear rate variations is much too low that the uncertainties in calculated target fracture slip velocities (of the order of 50% because of mesh and sampling frequency dependencies, cf Section 4.6) would be important /Börgesson et al. 2004/. The results found here are therefore consistent with the assumptions made in the buffer/canister earthquake study.

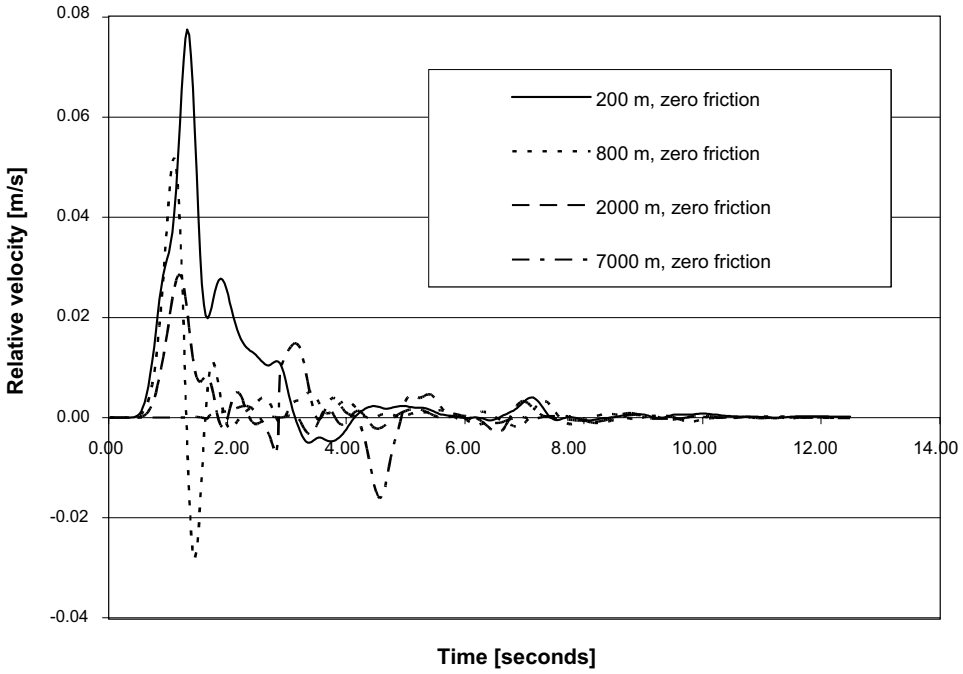

Figure 6-1. *Target fracture slip velocities in WAVE model. From /Munier and Hökmark 2004/.*

6.3 Induced target fracture slip

The key output parameter from the models was the maximum induced target fracture slip. These results were compared with the canister damage criterion presently applied by SKB. According to the criterion, a slip of more than 100 mm on a fracture intersecting a deposition hole would jeopardize the integrity of the canister/buffer system /SKB 1999/. From the results, the following can be concluded:

- The largest target fracture slip found in the models was 58 mm, i.e. well below the 100 mm criterion. This amount of slip was found in a target fracture located at 200 m distance from the primary fault in *Case B*. The maximum target fracture slip found in *Case A* was 46 mm.
- At 200 m fault distance, the average target fracture slip was about 17 mm for *Case A* and 29 mm for *Case B*. For *Case A,* 67% of all fractures at 200 m distance slipped less than 25% of the canister damage threshold. For *Case B* 50% slipped less than 25% of that threshold. The distance between the target fracture and the primary fault has great importance for the results. At 600 m and 1,000 m distance, the amounts of fracture slip were small. No fracture at 600 m distance or larger slipped by more than 25% of the threshold.
- There are large differences in the distribution of induced slip between different target fracture orientations. The maximum target fracture slip in *Case A* was found in a fracture with dip direction 90°, whereas the maximum in *Case B* was found in a fracture with dip direction 270°. This is a consequence of the very significant *Case A – Case B* difference in stress pattern at repository depth. This indicates that the fault geometry has importance for the amount of slip that is induced in different fracture sets.
- The primary fault slip results in static stress redistributions. The stress states at 200 m distance from the primary fault before and after the earthquake were compared. The results indicated that at one location (*Case A,* footwall side), the static stress redistribution itself would cause target fractures to slip (cf Figure 4-9). At all other locations studied, the stability margin increased as a consequence of the earthquake (Figure 4-9). The conclusion that can be drawn from this is that the static stress redistribution effects alone may be sufficient for inducing fracture slip at some locations. At other locations, however, where the effect of the strain energy release is to relax stresses and increase the fracture stability, slip may be induced by stress peaks and temporary strength reductions. At these locations, the dynamic effects are of great importance.

- The action of the stress wave seems to cause a temporary loss of strength and (or) a simultaneous temporary increase in shear stress. Comparing examples of target fracture slip histories with corresponding histories of shear stresses and normal stresses on hypothetical fracture planes shows that the slip coincides completely with short (less than seconds) periods of lost stability (Figure 4-10).

The amounts of target fracture slip found in the models analyzed here is smaller than those found in previous studies, where more conservative target fracture strength assumptions were made. /Munier and Hökmark 2004/, for instance, reported modeling results from analyses performed with the dynamic code WAVE. According to the WAVE results, a horizontal, frictionless target fracture with 100 m radius located at 200 m distance from the primary fault would slip by about 65 mm (Figure 6-2). The shear displacement of a fracture in an elastic homogenous medium depends linearly on the radius /Pollard and Segall 1987/. The 65 mm slip found for the 100 m radius fracture would then correspond to 98 mm of slip for 150 m radius fractures. This is 1.7 times more than the maximum slip found here for 150 m radius fractures at 200 m distance. This large difference is mainly due to the difference in target fracture shear strength. In the WAVE analysis, target fractures were arbitrarily and conservatively assumed to be frictionless whereas the 34° friction angle used in the present study is based on site data.

There are also differences in the target fracture orientations and in primary fault geometry. In the WAVE analysis the target fracture was horizontal whereas the maximum slip in the *3DEC* study occurred on fractures dipping 45°. Further, the primary fault in the WAVE model was vertical and buried. If the WAVE result instead is compared with the result from a horizontal *Case A*-target fracture, the induced slip on the WAVE target fracture is about 2.2 times that of the *Case A*-fracture.

At larger distances, the differences seem to be even more pronounced. According to Figure 6-2, the fracture at 800 m distance slips about 20 mm in the WAVE analysis. This would correspond to 30 mm for 150 m radius fractures, whereas the maximum slip found on the horizontal *3DEC* target fractures at 600 m and 1,000 m in *Case A* were 0.6 mm and 0.4 mm, respectively.

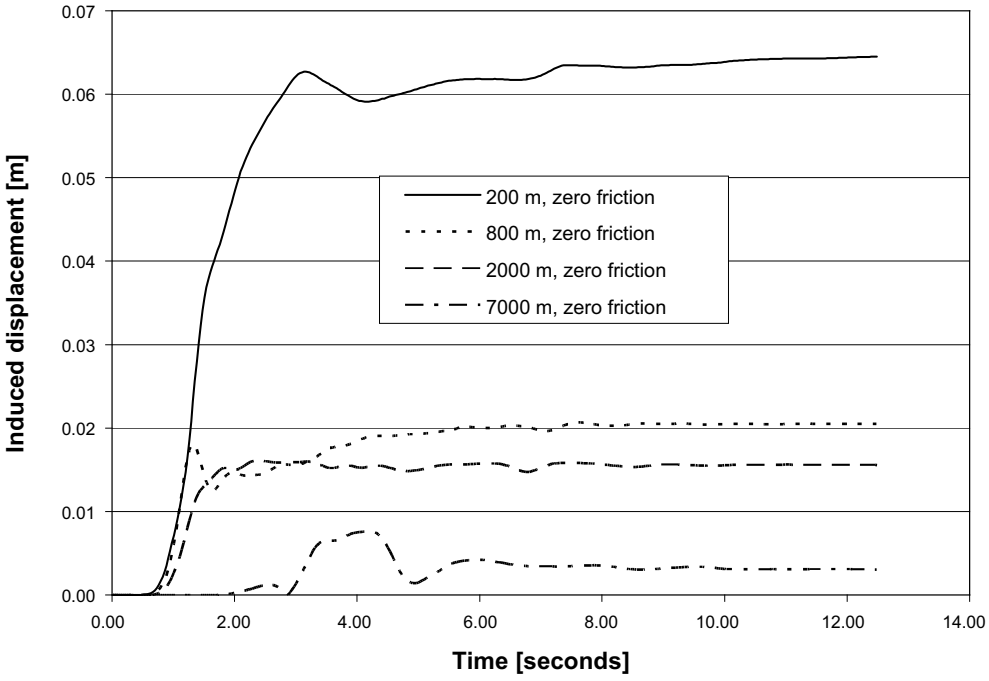

Figure 6-2. *Target fracture induced slip in WAVE analysis. The fractures were horizontal, frictionless, 100 m in radius and located at given distances from primary fault. From /Munier and Hökmark 2004/.*

6.4 Final remarks

The *3DEC* simulations gave considerably less target fracture displacements than corresponding previous WAVE and *FLAC3D* simulations. Fractures of 150 m radius can be allowed to intersect deposition holes at 200 m distance from potential earthquake faults capable of hosting earthquakes of at least magnitude 6 without risk of seismically induced canister damage. The major reason for the significantly smaller effects found in this study compared with previous studies is the use of more realistic target fracture properties. Yet many of the assumptions made here are well on the conservative side:

- The primary fault shear velocity appeared to be about twice the velocity reported for large earthquakes. This means that the particle velocity and consequently the stress wave amplitudes were overestimated. Reducing the stress wave amplitudes by 50% would significantly reduce the impact on the target fractures.
- The fault slip/magnitude ratio was between 5 and 10 times higher than the average according to data base regressions (Figure 5-3). This confirms that the stress drop, the particle velocity and consequently the stress wave amplitudes are likely to have been overestimated in comparison with typical average events (However, note that there are no slip-magnitude regressions for glacially induced earthquakes).

6.5 Further work

The effects of large earthquakes remain to be examined. An earthquake of magnitude 7 or 8 will have a larger range of influence compared with the magnitude 6 earthquakes considered here. This means that target fracture slip will not decrease with distance as rapidly as illustrated in Figure 4-13 for magnitude 6 events, i.e. distant target fracture will slip more. The behavior of nearby target fractures, however, is not determined by the total amount of released strain energy, but by the conditions at close parts of the earthquake fault. Therefore there is a possibility that the behavior of target fractures located close to the fault, for instance at 200 m distance, will be similar to the behavior found here for target fractures at that distance from magnitude 6 earthquakes. As far as effects of the static stress drop are concerned, this will always be true, provided that the stress drop can be assumed to be independent of magnitude as suggested by /Scholz 1990/.

The results in this study indicate, however, that the dynamic effects are important for triggering target fracture slip. Even if the average static stress drop in large earthquakes is equal to what was used in the present models (15 MPa), the fault slip velocity may be larger, which would give higher stress wave amplitudes and, potentially, more target fracture slip. If this should be regarded as a real concern is, however, uncertain since the fault slip velocities obtained here for M6 turned out to be higher than velocities reported for events of magnitude 7 and larger (cf Section 5.4).

The suggestions and considerations above need to be examined. Target fracture slip caused by magnitude 7 and magnitude 8 earthquakes should be calculated using the *3DEC* code. At present it is not possible to analyze dynamic models sufficiently large to fully accommodate a primary fault of about 500 km^2 (M7) or 8,000 km^2 (M8). Therefore, following steps should first focus on developing techniques to define reasonably relevant boundary conditions for truncated models, using the verified M6 models as benchmarks.

As noted in Section 5.5.1, there is a possibility that the shear rate has importance for the fracture shear resistance and that this can have importance for the amount of induced fracture slip. Furthermore, the discussion in Section 5.7 indicates the possibility that propagation of fractures can reduce the maximum fracture displacement. These issues may also be addressed in further studies.

7 References

Arvidsson R, 1996. Fennoscandian Earthquakes: Whole Crustal Rupturing Related to Postglacial Rebound. Science, Vol. 274, 744–746.

Barbero M, Barla G, Zaninetti A, 1996. Dynamic Shear strength of Rock Joints Subjected to Impulse Loading. International Journal of Rock Mechanics and Mining Science & Geomechanics Abstracts, Volume 33, Issue 2, February 1996, Pages 141–151.

Börgesson L, Johannesson L-E, Hernelind J, 2004. Earthquake induced rock shear through a deposition hole. Effect on the canister and the buffer. SKB TR-04-02, Svensk Kärnbränslehantering AB.

Fälth B, Hökmark H, 2006. Mechanical and thermo-mechanical discrete fracture near-field analyses based on preliminary data from the Forsmark, Simpevarp and Laxemar sites. SKB R-06-89, Svensk Kärnbränslehantering AB.

Hedin A, 2005. An analytic method for estimating the probability of canister/fracture intersections in a KBS-3 repository. SKB R-05-29, Svensk Kärnbränslehantering AB.

Hermanson J, Forssberg O, Fox A, La Pointe P, 2005. Statistical model of fractures and deformation zones. Preliminary site description, Laxemar subarea, version 1.2. SKB R-05-45, Svensk Kärnbränslehantering AB.

Itasca, 2003. *3DEC* – 3-Dimensional Distinct Element Code, User's Guide. Itasca Consulting Group, Inc., Minneapolis, USA.

La Pointe P, Wallman P, Thomas A, Follin S, 1997. A methodology to estimate earthquake effects on fractures intersecting canister holes. SKB TR-97-07, Svensk Kärnbränslehantering AB.

La Pointe P, Outters N, Follin S, 2000. Evaluation of the conservativeness of the methodology for estimating earthquake-induced movements of fractures intersecting canisters. SKB TR-00-08, Svensk Kärnbränslehantering AB.

La Pointe P, Olofsson I, Hermanson J, 2005. Statistical model of fractures and deformations zones for Forsmark. Preliminary site description Forsmark area – version 1.2. SKB R-05-26, Svensk Kärnbränslehantering AB.

Ma K-F, Brodsky E E, Mori J, Ji C, Song T-R A, Kanamori H, 2003. "Evidence for fault lubrication during the 1999 Chi-chi, Taiwan, earthquake (M (sub w) 7.6)." Geophysical Research Letters 30(5): 4.

Muir Wood R, 1993. A review of the seismotectonics of Sweden. SKB TR-93-13, Svensk Kärnbränslehantering AB.

Munier R, Hökmark H, 2004. Respect distances. Rationale and means of computation. SKB R-04-17, Svensk Kärnbränslehantering AB.

Pollard D D, Segall P, 1987. Theoretical displacements and stresses near fractures in rock: With applications to faults, joints, veins, dikes and solution surfaces. Fracture Mechanics of Rock. Academic Press Inc. Ltd., London.

Scholz C H, 1990. The mechanics of earthquakes and faulting. Cambridge University Press, United Kingdom.

Sekiguchi H, Horikawa H, Kase Y, Ishiyama T, Satake K, Sugiyama Y, Mizuno K, Pitarka A, 2004. Ground motion prediction in Osaka Basin, central Japan, based on geological, geophysical and paleoseismological data and numerical simulations of earthquake rupture and ground motion. Paper no. 1768, 13th World Conference on Earthquake Engineering. Vancouver, B.C, Canada, 2004.

SKB, 1999. Deep repository for spent nuclear fuel. SR 97 – Post-closure safety**.** SKB TR-99-06, Svensk Kärnbränslehantering AB.

SKB, 2005a. Preliminary site description. Simpevarp subarea – version 1.2. SKB R-05-08, Svensk Kärnbränslehantering AB.

SKB, 2005b. Preliminary site description. Forsmark area – version 1.2. SKB R-05-18, Svensk Kärnbränslehantering AB.

SKB, 2006. Preliminary site description. Laxemar subarea – version 1.2. SKB R-06-10, Svensk Kärnbränslehantering AB.

Stein S, Wysession M, 2003. An introduction to Seismology, Earthquakes, and Earth structure. Blackwell Publishing, Malden, USA.

Wald D J, Heaton T H, 1994. "Spatial and temporal distribution of slip for the 1992 Landers, California, earthquake." Bulletin of the Seismological Society of America 84(3): 668–691.

Wells D L, Coppersmith K J, 1994. New empirical relationships among magnitude, rupture length, rupture width, rupture area, and surface displacement. Bulletin of the Seismological Society of America. Vol. 84(4): p 974–1002.